







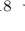


The Astrometric Animation of Water Masers towards the Mira Variable BX Cam

SHUANGJING XU ^{1,2} HIROSHI IMAI ^{3,4,5} YOUNGJOO YUN,¹ BO ZHANG,² MARÍA J. RIOJA ^{6,7,8}
RICHARD DODSON ⁶, SE-HYUNG CHO,⁹ JAEHEON KIM ¹, LANG CUI ¹⁰, ANDREY M. SOBOLEV ¹¹
JAMES O. CHIBUEZE ^{12,13}, DONG-JIN KIM,^{14,15} KEI AMADA,³ JUN-ICHI NAKASHIMA,¹⁶ GABOR OROSZ,¹⁷
MIYAKO OYADOMARI,³ SEJIN OH,¹ YOSHINORI YONEKURA ¹⁸, YAN SUN,^{2,19} XIAOFENG MAI,^{2,19} JINGDONG ZHANG,^{2,19}
SHIMING WEN,² AND TAEHYUN JUNG¹

¹*Korea Astronomy and Space Science Institute, 776 Daedeok-daero, Yuseong-gu, Daejeon 34055, Republic of Korea*

²*Shanghai Astronomical Observatory, Chinese Academy of Sciences, 80 Nandan Road, Shanghai 200030, China*

³*Graduate School of Science and Engineering, Kagoshima University,
1-21-35 Korimoto, Kagoshima 890-0065, Japan*

⁴*Amanogawa Galaxy Astronomy Research Center, Graduate School of Science and Engineering, Kagoshima University,
1-21-35 Korimoto, Kagoshima 890-0065, Japan*

⁵*Center for General Education, Institute for Comprehensive Education, Kagoshima University,
1-21-30 Korimoto, Kagoshima 890-0065, Japan*

⁶*ICRAR, M468, The University of Western Australia, 35 Stirling Hwy, Crawley, Western Australia, 6009, Australia*

⁷*CSIRO Astronomy and Space Science, PO Box 1130, Bentley WA 6102, Australia*

⁸*Observatorio Astronómico Nacional (IGN), Alfonso XII, 3 y 5, 28014 Madrid, Spain*

⁹*Astronomy program, Department of Physics and Astronomy, Seoul National University, Seoul 08826, Republic of Korea/Korea
Astronomy and Space Science Institute, Yuseonggu, Daejeon 34055, Republic of Korea*

¹⁰*Xinjiang Astronomical Observatory, Chinese Academy of Sciences, 150 Science 1-Street, Urumqi 830011, China*

¹¹*Ural Federal University, 19 Mira Street, 620002 Ekaterinburg, Russia*

¹²*Centre for Space Research, North-West University, Potchefstroom 2520, South Africa*

¹³*Department of Physics and Astronomy, Faculty of Physical Sciences,
University of Nigeria, Carver Building, 1 University Road, Nsukka, Nigeria*

¹⁴*Massachusetts Institute of Technology Haystack Observatory, 99 Millstone Road, Westford, MA 01886, USA*

¹⁵*Max-Planck-Institut für Radioastronomie, Auf dem Hügel 69, D-53121 Bonn, Germany*

¹⁶*School of Physics and Astronomy, Sun Yat-sen University, 2 Daxue Road, Tangjia, Zhuhai, Guangdong Province, China*

¹⁷*Joint Institute for VLBI ERIC, Oude Hoogeveensedijk 4, 7991PD Dwingeloo, Netherlands*

¹⁸*Center for Astronomy, Ibaraki University, 2-1-1 Bunkyo, Mito, Ibaraki 310-8512, Japan*

¹⁹*University of Chinese Academy of Sciences, No.19 (A) Yuquan Rd. Shijingshan, Beijing, 100049, China*

ABSTRACT

We report VLBI monitoring observations of the 22 GHz water (H₂O) masers around the Mira variable BX Cam, which were carried out as a part of the EAVN Synthesis of Stellar Maser Animations (ESTEMA) project. Data of 37 epochs in total were obtained from 2018 May to 2021 June with a time interval of 3–4 weeks, spanning approximately three stellar pulsation periods ($P \sim 440$ d). In particular, the dual-beam system equipped on the VERA stations was used to measure the kinematics and parallaxes of the H₂O maser features. The measured parallax, $\pi = 1.79 \pm 0.08$ mas, is consistent with *Gaia* EDR3 and previously measured VLBI parallaxes within a 1- σ error level. The position of the central star was estimated, based on both the *Gaia* EDR3 data and the center position of the ring-like 43 GHz silicon-monoxide (SiO) maser distribution imaged with the KVN. The three-dimensional H₂O maser kinematics indicates that the circumstellar envelope is expanding at a velocity of 13 ± 4 km s⁻¹, while there are asymmetries in both the spatial and velocity distributions of the maser features. Furthermore, the H₂O maser animation achieved by our dense monitoring program manifests the propagation of shock waves in the circumstellar envelope of BX Cam.

Keywords: masers—stars: individual (BX Cam)—stars:evolved, astrometry, kinematics, radio interferometer

1. INTRODUCTION

The long-period variables (LPVs), such as Mira variables, are stars of low to intermediate masses which have reached the late evolutionary stage of Asymptotic Giant Branch (AGB) phase. They are characterised by long-period (>100 d) variations in radius, brightness, and temperature, which are caused by stellar surface instability and radial pulsation (see the latest catalogue of [Lebzelter et al. 2022](#)). These stars also have an intense mass-loss phenomenon or a superwind, which leads to formation of a circumstellar envelope (CSE) made of gas and dust (see the review of [Höfner & Olofsson 2018](#)).

The stellar mass loss may be driven, primarily, by the pressure from the stellar radiation on dust grains, while pulsation-induced shocks are expected to enhance the mass loss (e.g., [Habing & Olofsson 2004](#); [Höfner 2011](#); [Höfner et al. 2016](#)). In addition, the stellar structure is basically spherically symmetric, while the mass loss often exhibits significant asymmetry on very different spatial ($1\text{--}10^4$ AU) and temporal (a few months to a few 10^4 years) scales ([Höfner & Olofsson 2018](#)). The mass loss asymmetry observed in the vicinity of the stellar surface (e.g., [Khouri et al. 2020](#)) might be linked to the existence of giant gas segments created from convection in the stellar interior. It is interesting to trace how such asymmetry will grow while the gas segments are being accelerated outward. It is likely that the mechanism of dust acceleration in the CSE, the enhancement of the outward flow, and the growth of its asymmetry may be dependent on the property or abundance of the ejected materials (i.e., carbon-rich or oxygen-rich composition) ([Höfner & Olofsson 2018](#)).

Circumstellar SiO and H₂O masers are located at, respectively, $\sim 2\text{--}4$ stellar radii (e.g., [Diamond et al. 1994](#)) and $\sim 5\text{--}50$ stellar radii (e.g., [Richards et al. 2012](#)) of a typical oxygen-rich AGB star, while the dust formation layer is co-located between the SiO masers and H₂O masers ([Habing 1996](#); [Wittkowski et al. 2007](#)). The location of SiO masers corresponds to the innermost part of the CSE, where molecules are still rich and outward and inward motions are often observed (e.g. [Gonidakis et al. 2013](#)). The location of H₂O masers corresponds to the zone of the outward acceleration of dust and gas, where molecular gas is cooled and condensed to dust while H₂O molecules are still enriched. The maser structures are composed of clusters of compact maser features (isolated gas clumps with sizes of ~ 1 AU). This enables us to measure the three-dimensional velocity field of the CSE through monitoring observations by Very Long Baseline Interferometry (VLBI) with excellent angular resolution (e.g., [Imai et al. 2003](#)). Groups of maser features may trace giant gas/dust clumps, whose origins have been debated in terms of the convection of the stellar interior or just instability on the stellar surface ([Höfner & Olofsson 2018](#)). Thus, the maser spatio-kinematics have direct relationship to such gas/dust dynamics and can illuminate important issues on the mechanisms of maser excitation.

The EAVN Synthesis of Stellar Maser Animations (ESTEMA) project has been conducted as one of the KaVA (a combined array of the Korean VLBI Network, KVN, and Japanese VLBI Exploration of Radio Astrometry, VERA) Large Program projects followed by a series of General Proposal projects of the East Asian VLBI Network (EAVN), aiming at intensive VLBI monitoring observations of CSE masers associated with LPVs of different pulsation periods (300—1000 d) over a few stellar pulsation cycles. EAVN is suitable for high cadence VLBI monitoring because more than six telescopes are always available for imaging of CSE masers. The typical angular resolutions are $1.2(\text{K})/0.6(\text{Q})$ mas with the core array KaVA, and the largest detectable angular scales are $9(\text{K})/5(\text{Q})$ mas with the short baselines of ~ 300 km provided by KVN. The expected image sensitivities are $\sim 30(\text{K})/50(\text{Q})$ mJy beam⁻¹ for KaVA and $\sim 40(\text{K})/60(\text{Q})$ mJy beam⁻¹ for KVN, with an integration time of 4 hours and narrower bandwidth of 15.625 kHz for maser emission. In particular, it enables us to simultaneously monitor four to eight lines of H₂O and SiO masers at four frequency (22/43/86/129 GHz or K/Q/W/D) bands with the KVN. Absolute positions, proper motions of maser gas clumps, and the annual parallax of the maser source system can be determined by precise astrometry with the dual-beam system of VERA. The animation of circumstellar masers would demonstrate in detail the behaviors of maser emission, reflecting the dynamics of the maser clumps and variation in regions of maser excitation around the LPVs.

Here we present the first result of ESTEMA, which has been derived from H₂O masers associated with the Mira variable star BX Camelopardalis (BX Cam). This star is an oxygen-rich Mira variable with similar, but slightly

inconsistent, reported pulsating periods of 486 d (AAVSO)¹ or 440 d (Matsuno et al. 2020). The spectral type is M9.5 (Solf 1978), and the presence of bright SiO, H₂O, and OH masers have been confirmed (Ukita & Le Squeren 1984; Matsuno et al. 2020). The trigonometric parallax and the spatial distribution of H₂O masers with three collimated flows have been reported by Matsuno et al. (2020). This star was selected as one of the ESTEMA targets because of the more flexible allocation of VLBI observation sessions for this Northern-sky star. Similarly to the intensive monitoring observations of SiO ($v=1, J=1\rightarrow 0$) masers around TX Cam with the Very Long Baseline Array (VLBA) (Diamond & Kemball 2003; Gonidakis et al. 2010, 2013), the present monitoring project enables us to elucidate the global behaviour of an example of CSE H₂O masers for the first time. CSE H₂O masers also should be physically related to the stellar pulsation because of the periodic variation in the maser spectra (Shintani et al. 2008; Kim et al. 2014). However, the true origin of such a maser behavior can be visualized by an animation of the VLBI images. The astrometry on the maser animation is crucial to exactly trace the motions of the individual maser features. After subtracting maser position modulations due to the annual parallax and the secular motion of the maser source system, the maser maps can be registered on the reference frame, which then provides a fixed frame that can be compared with the location of the pulsating star whose astrometric data is now available from the *Gaia* Early Data Release 3 (*Gaia* EDR3) (Gaia Collaboration et al. 2021). A maser animation derived based on above astrometric steps enable us to visualize a radial expansion of the CSE masers and some deviations of the maser motions from constant-velocity motions, such as radial accelerations, rotations, etc.

2. OBSERVATIONS AND DATA REDUCTION

The monitoring observations of H₂O and SiO masers around BX Cam in ESTEMA have been ongoing since 2018 May, except in the EAVN maintenance season (June–August). The EAVN telescopes that have participated in ESTEMA observations include four telescopes of VERA (Mizusawa, Iriki, Ogasawara, and Ishigakijima), three telescopes of the KVN (Yonsei, Ulsan, Tamna), two telescopes of the Chinese VLBI Network (CVN: Tianma, Urumqi in K-band only), and one Japanese telescope (Takahagi in K-band only). The time cadence for a single observational epoch is 3–4 weeks, which is approximately equal to a time resolution of 1/20 stellar pulsation cycles of BX Cam (~ 22 d). Each observation epoch corresponds to a pair of K and Q-band experiments over two consecutive days and lasts for 8 hr (2 d \times 4 hr). We have designed the observations to use all of the unique capabilities of the KVN and VERA in EAVN, using a hybrid setup of simultaneously monitoring H₂O (22.235080 GHz) and SiO (42.820539, 43.122027, 86.243442, and 129.363358 GHz) maser lines and conducting high-accuracy astrometry by observing the maser and the reference continuum sources simultaneously.

In this paper, we mainly focus on the K-band data as listed in Table 1, spanning observations from 2018 to 2021. The data sample has crossed three light curve maxima of the stellar pulsation from phase ϕ 0.65 to ϕ 3.17. Each of the observation sessions had a duration of 4 hr including scans on the target, BX Cam, the fringe finder, NRAO150, and the delay calibrator, J0721+7120 ($\alpha_{J2000} = 07^{\text{h}}21^{\text{m}}53^{\text{s}}.4485\pm 0.31$ mas, $\delta_{J2000} = 71^{\circ}20'36''.363\pm 0.10$ mas). We alternated scans between BX Cam for 7 min and the calibrator for 2 min. The angular separation between these two sources is 7.9° on the sky, which is suitable for source-frequency phase-referencing (SFPR) analysis with KVN data (Dodson et al. 2014). Meanwhile, the phase reference source J0524+7034 ($\alpha_{J2000} = 05^{\text{h}}24^{\text{m}}13^{\text{s}}.4333\pm 0.39$ mas, $\delta_{J2000} = 70^{\circ}34'52''.906\pm 0.13$ mas²), 2.0° away from the target, was observed by the second beam of VERA to determine the absolute positions of the maser spots of BX Cam.

The received signals in left circular polarization were recorded in all the EAVN stations with 16 base-band channels (BBCs) each with a bandwidth of 16 MHz, one of which includes the maser emission of BX Cam. In VERA, 15 BBCs were assigned to the signals received by the second beam so as to cover a total width of 496 MHz. The recorded signal data were correlated using three passes with the hardware correlator in Daejeon, Korea (Lee et al. 2015). The first pass was processed for the BBC including H₂O masers with all EAVN antennas and yielded 2048 spectral channels, corresponding to a velocity spacing of 0.105 km s⁻¹ at 22.235 GHz. The second pass was processed for the phase reference source J0524+7034 observed by the second beam of VERA. The third pass was for simultaneously monitoring of H₂O and the four SiO maser lines using the KVN. In this pass, all of the 16 BBCs were processed with 1024 spectral channels per BBC.

¹ <https://www.aavso.org>

²

The quasar positions are cited from http://astrogeo.org/sol/rfc/rfc_2021d/.

The data calibration was performed with the Astronomical Image Processing System (AIPS) (Greisen 2003) developed by the National Radio Astronomy Observatory (NRAO). We have developed the pipeline scripts with Parsel-Tongue (Kettenis et al. 2006) for ESTEMA project. A priori amplitude calibration was done using the system noise temperatures and antenna gains logged during observations at KVN and VERA stations. These system noise temperatures were measured with the chopper-wheel method (Ulich & Haas 1976) and were evaluated using the ‘‘R-Sky’’ method (Honma et al. 2004), by observing a reference black body. Since the system temperature measurements were absent for Tianma, Urumqi, and Takahagi stations, we applied the template spectrum method (Reid 1999), in which a template spectrum of the H₂O maser emission was obtained from the auto-correlation data. The estimated amplitude calibration errors of both methods were less than 10% for EAVN (Cho et al. 2017). For imaging the H₂O masers with all the EAVN antennas, the velocity channel including a bright, single, and compact maser spot was selected as the reference for fringe fitting and self-calibration. The detection limit was typically 0.4 Jy beam⁻¹ at a 5- σ noise level, in maps without bright maser emission.

For astrometry with VERA, the instrumental relative delays between the dual beams measured by the horn-on-dish method are applied (Honma et al. 2008) and the delay re-calculation tables (Nagayama et al. 2020) were used. In the delay re-calculation tables, the more accurate delay models were updated, with: the tropospheric zenith delay measured by the Global Positioning System (GPS), the ionospheric Total Electron Content (TEC) of the Global Ionosphere Map (GIM) produced by the Center for Orbit Determination in Europe (CODE), the station position measured in the monthly geodetic VLBI observations, and the updated maser positions (Nagayama et al. 2020, and the references therein). Then we used J0524+7034 as the phase reference source to determine the absolute position of masers. 5 σ noise levels of the phase referenced map of VERA data are typically 1.0 Jy beam⁻¹. Therefore, we can measure the absolute positions of the bright masers of BX Cam with the VERA dual-beam bona-fide astrometry, then propagate this to all of the maser spots in the EAVN image by registering the bright masers in the pair of images. We used the SFPR technique described in Dodson et al. (2014) to obtain the astrometric registration of the H₂O and SiO maser spots from the KVN data.

3. RESULTS

3.1. Periodic variation of the H₂O maser spectra

Frequent observations, as well as the time-span of ESTEMA, allow us to study the variability and periodicity of maser intensity on timescales of a few weeks to a few years in terms of the possible correlation with stellar pulsation (Gonidakis et al. 2010). Figure 1 demonstrates the changes in the spectrum with time. Since some of imaging observations of the masers failed and some of the maser images are made by different array configurations, we use the maser intensity on the KVN stations for spectral analysis, e.g., making cross-power spectra on a short baseline in Figure 1, making the total-power spectra on each KVN stations, and analysing the period and phase of the spectra.

The excitation of H₂O masers is sensitive to both the dynamics of a stellar wind and the stellar radiation with periodic variation. The previous monitoring observations of H₂O masers around BX Cam with the VERA Iriki telescope (Shintani et al. 2008; Matsuno et al. 2020) did not determine the period and phase lag of the H₂O maser variability.

Multiple estimates of the optical period of BX Cam have been reported by the American Association of Variable Star Observers (AAVSO) and Matsuno et al. (2020). AAVSO reported a period of 486 d³ without the details of the specific time range of data or a specific method. Matsuno et al. (2020) determined a period of 440 d using the 40 nights in AAVSO database between 2016 February and 2019 December. We also reanalysed 54 nights from the AAVSO database at V-band from 2016 February to 2021 October using two methods. One is the Date Compensated Discrete Fourier Transform (DC DFT) method with the popular analysis tool VStar (Benn 2012), and another is the Lomb-Scargle Periodogram (Lomb 1976; Scargle 1982; VanderPlas 2018), which is equivalent to least-squares fitting of sine waves. We obtained an averaged optical period of 440 \pm 5 d using the two methods as shown in Figure 2, which is consistent with Matsuno et al. (2020).

During the period from $\phi = 0.65$ to 3.17 in stellar light curve phase, the H₂O masers have continuously been found at a local-standard-of-rest velocity (V_{LSR}) range from -7 to -16 km s⁻¹. We also detected the red-shifted component at $V_{\text{LSR}}=7-10$ km s⁻¹ around the light maxima: from $\phi = 1.00$ to 1.32 and from $\phi = 1.88$ to 2.14, which has also been found in previous observations by Engels et al. (1988) and Matsuno et al. (2020). The peaks of the H₂O maser

³ <https://www.aavso.org/vsx/index.php?view=detail.top&oid=4634>

Table 1. EAVN observations of BX Cam at K band

Obs. Code	Epoch	MJD ^a	Optical Phase(ϕ) ^b	Stations ^c	Num. ^d	RMS ^e	High-Res. ^d Imaging	VERA ^d Astrometry	Problem ^f
k18hi01a	2018-05-24	58262	0.65	VmVrVoVsKyKuKt	1	283			
k18hi01c	2018-06-06	58275	0.68	VmVrVoVsKyKuKt	1	320			
k18hi01e	2018-09-03	58364	0.88	VmVrVoVs KuKt	2	278			
k18hi01g	2018-10-07	58398	0.96	VrVoVsKyKuKt	0	1513			Kt(N), KyKu(R)
k18hi01i	2018-10-24	58415	1.00	VmVrVoVsKyKuKt Ur	13	210	✓		KyKuKt(R)
k18hi01k	2018-11-11	58433	1.04	VmVrVoVsKyKuKtT6Ur	16	122	✓	✓	T6Ur(N)
k18hi01m	2018-12-16	58468	1.12	VmVrVoVsKyKuKt	21	83	✓	✓	
k18hi01o	2019-01-17	58500	1.19	VmVrVoVsKyKuKtT6	15	62	✓	✓	
k19hi01a	2019-02-11	58525	1.25	VmVrVoVsKyKuKt	17	89	✓		Vm(N)
k19hi01c	2019-03-14	58556	1.32	VmVrVoVsKyKuKt	12	96			
k19hi01e	2019-04-11	58584	1.38	VmVrVoVsKyKuKt	5	123			
k19hi01g	2019-05-08	58611	1.44	VmVrVo KyKuKt	7	98			
a19hi03a	2019-09-07	58733	1.72	VmVr Vs KuKtT6	0	1461			T6(N)
a19hi03c	2019-10-10	58766	1.79	VmVr VsKy KtT6	6	154	✓		VmKy(N)
a19hi03e	2019-10-24	58780	1.83	VmVr VsKyKuKt	19	128	✓		
a19hi03g	2019-11-18	58805	1.88	VmVrVoVsKyKuKtT6	23	61	✓	✓	
a19hi03i	2019-12-16	58833	1.95	VmVrVoVsKyKuKtT6	32	65	✓	✓	
a19hi03l	2020-01-10	58858	2.00	VmVrVoVsKyKuKtT6	35	52	✓	✓	
a2004a	2020-02-07	58886	2.07	VmVrVoVsKyKuKt	38	57	✓	✓	
a2004c	2020-03-11	58919	2.14	VmVrVoVsKyKuKt	28	53	✓	✓	
a2004e	2020-03-27	58935	2.18	VmVrVoVs KuKtT6Ur	16	97	✓	✓	
a2004g	2020-04-20	58959	2.23	VmVrVoVsKyKuKt Ur	9	94	✓	✓	Ku(N)
a2004i	2020-05-13	58982	2.29	VmVrVoVsKy Kt Ur	12	88	✓	✓	
a2004k	2020-06-09	59009	2.35	VmVrVo KyKuKt Ur	11	136			
a2019a	2020-09-15	59107	2.57	Vm VoVsKyKu Ur	0	765			Vs(N)
a2019c	2020-09-24	59116	2.59	VmVrVoVsKyKuKt Ur	0	456			
a2019e	2020-10-18	59140	2.64	VrVoVsKyKuKt Ur	4	167			
a2019g	2020-11-12	59165	2.70	VrVoVsKyKuKt	6	97			
a2019i	2020-11-26	59179	2.73	VmVrVoVsKyKuKt Tk	6	128			
a2019m	2021-01-12	59226	2.84	VmVrVoVs KuKt Tk	7	93			
a2102a	2021-02-01	59246	2.89	VmVrVoVsKyKuKt Tk	15	68	✓		
a2102c	2021-02-19	59264	2.93	VmVrVoVsKyKuKt Tk	21	51	✓	✓	
a2102e	2021-03-12	59285	2.97	VmVrVoVsKyKu Tk	7	183	✓	✓	KyKu(R)
a2102g	2021-04-05	59309	3.03	VmVrVoVsKy KtT6UrTk	9	176	✓	✓	KyKt(R)
a2102i	2021-04-17	59321	3.06	VmVrVoVsKyKuKt Tk	6	598	✓		Ky(N), KuKt(R)
a2102k	2021-05-12	59346	3.11	VmVrVoVsKyKuKt Tk	14	439	✓		KyKuKt(R)
a2102m	2021-06-07	59372	3.17	VmVrVoVsKyKuKtT6Ur	16	111	✓		Ur(N)

^aMJD: Modified Julian Day.^bThe optical phase is estimated in Figure 2 using a mean period 440 days, optical maximum at 2020-01-08 and an uncertainty about 4 days.^cStation codes represent VERA-Mizusawa(Vm), VERA-Iriki(Vr), VERA-Ogasawara(Vo), VERA-Ishigakijima(Vs), KVN-Yonsei(Ky), KVN-Ulsan(Ku), KVN-Tamna(Kt), Tianma(T6), Urumqi(Ur), and Takahagi(Tk), respectively.^dThe purposes of the data sets: (1) “Num.”: Number of the maser features identified. (2) “High-Res. Imaging”: The images made including >2000 km baselines, which are used for analysing the maser features and relative proper motions. (3) “VERA Astrometry”: Phase-referencing astrometry with VERA dual-beam system, which are used for determining the absolute positions, absolute proper motions and annual parallaxes.^eNoise level (1- σ) of EAVN images in mJy beam⁻¹.^f(N): No fringe detection. (R) RCP: polarization fault due to wrong observation in right-hand circular polarization.

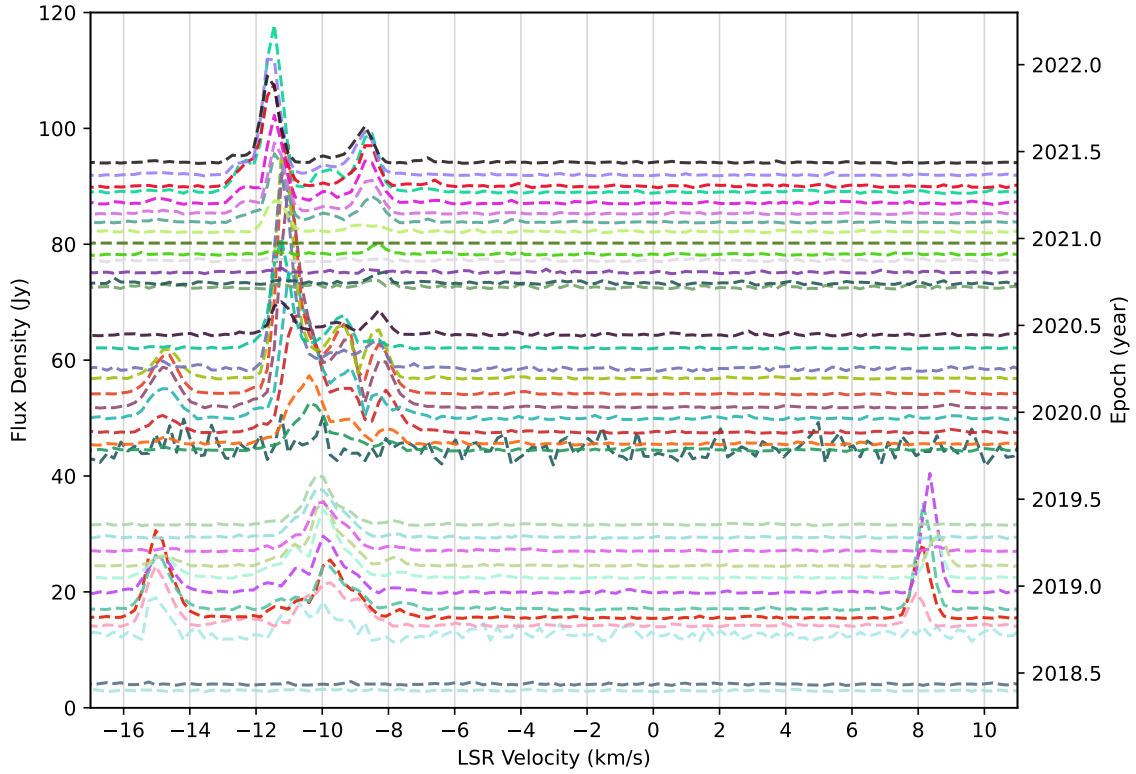


Figure 1. The cross power H_2O maser spectra on the Ky–Ku baseline (305 km). Few epochs on Ky–Kt baseline (476 km) when Ku is not available. All of the 37 epochs data were used.

intensity appeared at the epoch 2018-10-24 (ϕ 1.00), 2020-01-10 (ϕ 2.00), and 2021-04-05 (ϕ 3.03), while the peaks of optical intensity appeared at the epoch 2018-09-16 (ϕ 0.91), 2020-01-09 (ϕ 2.00), and 2021-02-27 (ϕ 2.94). Thus the peaks of the H_2O maser intensity have an average delayed time-lag $\sim 25 \pm 9$ days or phase-lag $\sim 0.06 \pm 0.02$ related to the peaks of optical intensity. The averaged time interval of H_2O maser peak intensity is $\sim 447 \pm 11$ days, which is a better fit to the period 440 d than 486 d (AAVSO).

The observed properties of the spectral and flux variability for the H_2O masers are as follows. (1) The H_2O masers are highly variable so that no maser components were detected in some of the maser flux minimum. (2) The maser flux and the optical magnitude exhibit a similar sinusoidal pattern, showing that the maser flux follows the pulsation of the star (same as the SiO masers [Gonidakis et al. 2010](#)). (3) The maxima of the periodic maser flux variation do not have a constant magnitude. (4) Time lags of the maser flux maxima with respect to the optical light maxima are also expected, but they are not necessarily constant as seen in the data (same as for the SiO masers [Gonidakis et al. 2010](#)). (5) The maser flux variations do not follow a specific pattern. The number of spectral features, as well as their fluxes, change not only during a single cycle but also from one cycle to another. (6) Systematic radial velocity drifts in the maser features are also found as shown on the spectrum.

3.2. The mapped H_2O maser features

Figure 3 shows the comparison between the maser brightness distributions taken with KVN, VERA and EAVN (KVN+VERA+T6) on 2020Jan10 ($\phi=2.00$). KVN is helpful to detect extended structures, while EAVN can detect a larger number of isolated compact maser features. VERA can measure the bona-fide positional information of bright masers using the dual-beam astrometric system. The H_2O masers were spatially well resolved into individual maser features with the EAVN synthesized beam. The image including Urumqi baselines shows no obvious difference, since only the brightest and compact maser features located at the map origin were detected on > 3000 km long baselines.

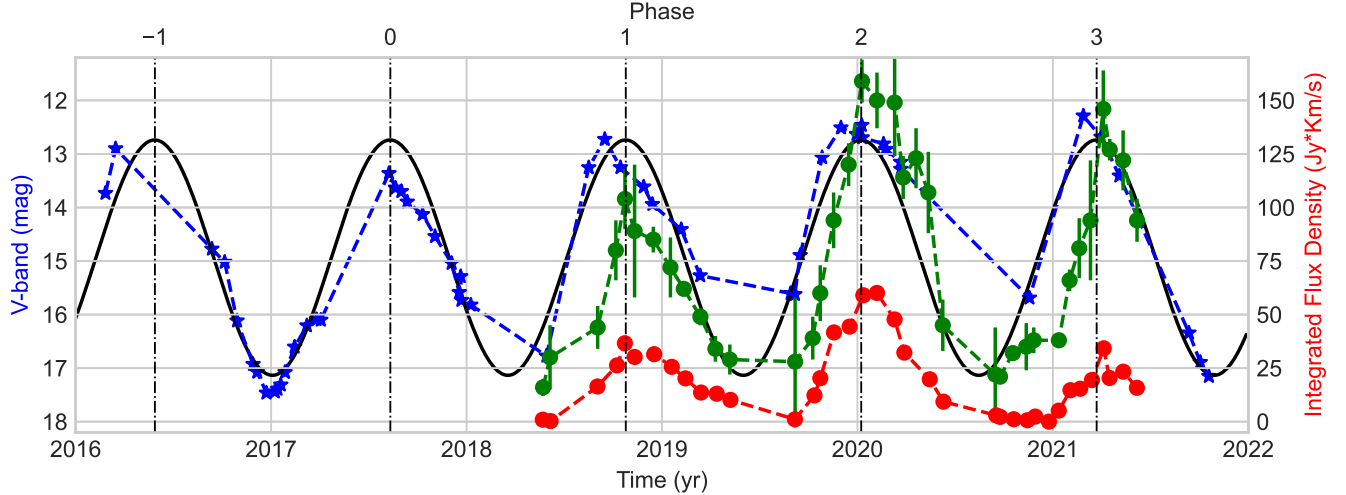


Figure 2. Integrated flux curves of 22 GHz H₂O masers from the cross (red circles) and total (green circles) power spectra of the KVN and V-band optical light curve (blue stars) from the AAVSO monitoring data. The total power spectra is using the weighted average of three KVN antennas (Kt,Ky,Ku), while the cross power spectra is using the short baselines as shown in Figure 1. The V_{LSR} velocity range for estimating the integrated flux densities is from -16 to -7 km s⁻¹ and from 7 to 10 km s⁻¹. At K band, the beam size of the KVN single-dish telescope is ~ 130 mas and the synthesized beam size of the projected KYS-KUS baseline is ~ 11 mas for BX Cam. The black solid line shows the sinusoidal fit to the optical light curve with a period of 440 d.

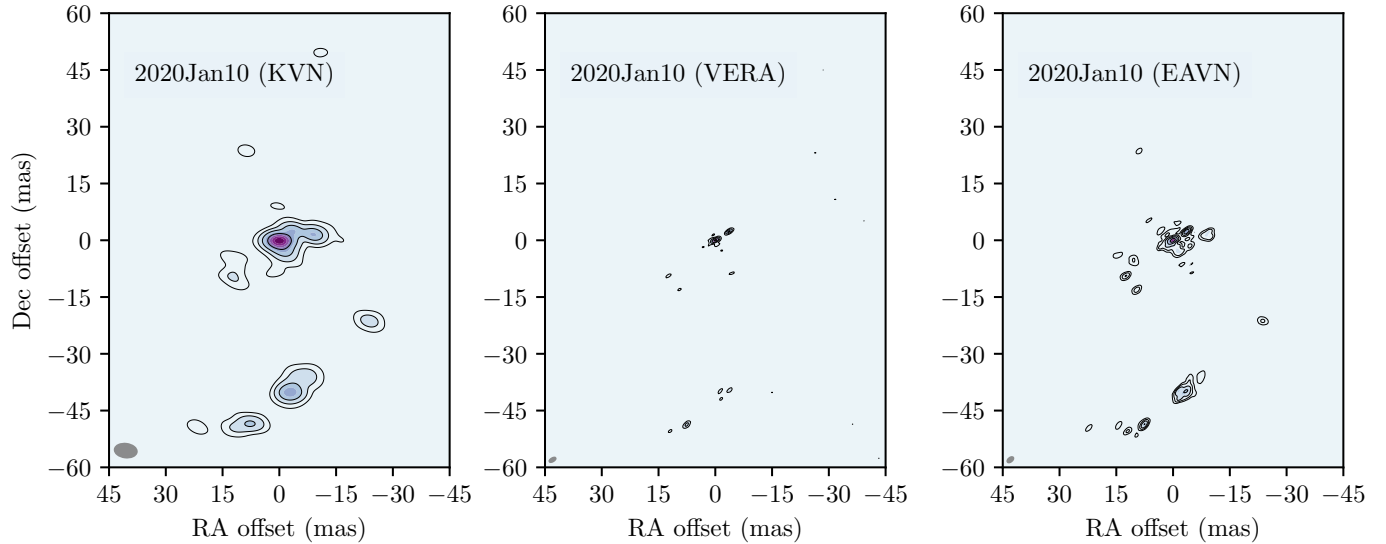


Figure 3. Left to Right: Moment-zero maps of the water maser emission in BX Cam from KVN, VERA, and EAVN (KVN+VERA+T6) observations at the same epoch, Jan 10, 2020. The maps are from images created by collapsing each spectral line cube to a single plane using the AIPS task SQASH, taking the weighted averages of each pixel. An ellipse in the bottom-left corner of each panel indicates the synthesized beam pattern of the image synthesis. The contour map is drawn with contour levels of $3, 6, 12, 24, \dots \times \sigma$, where 1σ corresponds to 0.03 Jy beam⁻¹(KVN), 0.04 Jy beam⁻¹(VERA), and 0.03 Jy beam⁻¹(EAVN), respectively.

The AIPS task SAD was used to extract maser spots information, e.g., positions and brightness, from the EAVN image data cube. For the component identification, a non-constant Gaussian was used and features with flux higher than six times the noise level were accepted. Maser feature candidates were identified as components if found in more than three consecutive channels within the cube (Gonidakis et al. 2010). Table 1 gives the possible numbers of maser features detected at individual epochs. We traced the relative positions and radial velocities of maser features at

different epochs, which had been stable from one epoch to another within 1 km s^{-1} in LSR velocity and within $6 \text{ mas yr}^{-1} \times \Delta t \text{ yr}$ in position. The Δt is the time gap between two epochs and the limit corresponds to the maximum movement velocity in Table 2. In practice it is difficult to automatically cross-identify components just relying on the above velocity and position window, thus we identified the components manually.

Figure 4 shows the example of internal structures of the maser features. Among them, 17 maser features with the lifespan longer than one Cycle are labelled with their identifier (MF#). Each maser feature is composed of a compact bright part and an extended structure. There are “spoke-like” (linearly distributed) (Zhang et al. 2012) maser features at all epochs. These maser features appear to be composed of gas flowing outward from the central star and mostly have decreasing (blue-shifted) or increasing (red-shifted) radial velocities.

Table 2. The radial velocity drifts and relative proper motions of the maser features

MF ^a	Cycle ^b	Radial Velocity ^c	RV Drift ^d	RA offset ^c	Rel μ_x ^e	Dec offset ^c	Rel μ_y ^e
ID	Fitting	km s ⁻¹	km s ⁻¹ yr ⁻¹	mas	mas yr ⁻¹	mas	mas yr ⁻¹
MF1	2+3	-11.25±0.04	-0.25±0.05	-0.02±0.01	0.03±0.01	0.02±0.01	-0.02±0.01
	2	-11.23±0.06	-0.38±0.27	-0.02±0.01	0.04±0.06	0.03±0.01	-0.09±0.04
MF2	1+2+3	-9.34±0.03	-0.35±0.04	-3.53±0.01	0.10±0.02	2.18±0.02	0.11±0.03
	2	-9.29±0.03	-0.70±0.19	-3.55±0.01	0.31±0.07	2.20±0.02	0.31±0.12
MF3	1+2	-14.78±0.03	0.17±0.05	-9.08±0.05	0.34±0.09	1.44±0.04	-0.77±0.06
	2	-14.79±0.04	0.31±0.28	-9.09±0.08	0.74±0.55	1.47±0.06	-1.19±0.40
MF4	1+2	9.07±0.06	0.79±0.06	-23.67±0.16	-1.20±0.09	-21.26±0.09	-0.78±0.10
	2	9.04±0.04	0.75±0.35	-23.70±0.08	-0.49±0.65	-21.34±0.04	-0.32±0.35
MF5	1+2+3	-6.95±0.05	-0.20±0.09	-7.46±0.11	-0.72±0.19	-35.87±0.12	-2.25±0.21
	2	-6.89±0.11	-0.33±0.77	-7.48±0.23	-1.39±1.56	-35.85±0.24	-3.90±1.64
MF6	1+2+3	-8.32±0.02	-0.32±0.04	-2.75±0.08	-0.48±0.13	-39.83±0.09	-3.75±0.15
	2	-8.32±0.03	-0.73±0.17	-2.67±0.12	0.34±0.61	-39.94±0.13	-4.30±0.70
MF7	1+2+3	-11.87±0.03	-0.38±0.06	7.60±0.01	0.64±0.01	-48.59±0.04	-3.08±0.07
	2	-11.84±0.04	-0.68±0.24	7.62±0.01	0.47±0.05	-48.63±0.05	-3.25±0.27
MF8	1+2+3	-10.86±0.04	-0.27±0.04	9.77±0.03	1.50±0.03	-51.22±0.03	-4.82±0.03
	2	-10.77±0.08	-0.54±0.40	9.75±0.10	1.75±0.47	-51.34±0.09	-4.97±0.44
MF9	1+2+3	-11.31±0.03	0.01±0.04	11.91±0.03	1.24±0.05	-50.25±0.02	-3.65±0.04
	2	-11.34±0.04	0.20±0.21	11.95±0.04	1.13±0.19	-50.37±0.03	-3.41±0.16
MF10	1+2	-11.58±0.03	-0.31±0.05	14.25±0.03	1.30±0.05	-48.84±0.03	-3.46±0.06
	2	-11.56±0.04	-0.48±0.26	14.27±0.05	1.10±0.27	-48.84±0.05	-3.48±0.30
MF11	1+2	-12.86±0.04	-0.31±0.06	22.18±0.04	2.78±0.05	-49.47±0.05	-4.26±0.07
	2	-12.85±0.04	-0.50±0.32	22.21±0.02	2.21±0.16	-49.52±0.02	-3.29±0.17
MF12	1+2	-11.87±0.32	0.00±0.31	23.88±0.12	3.29±0.12	-47.21±0.16	-4.34±0.15
	1	-11.87±0.83	0.00±0.80	23.45±0.31	2.88±0.29	-47.08±0.40	-4.21±0.39
MF13	2+3	-8.20±0.04	-0.49±0.05	9.57±0.03	1.31±0.03	-13.12±0.03	-0.66±0.04
	2	-8.13±0.05	-1.01±0.26	9.53±0.02	1.66±0.10	-13.07±0.05	-1.01±0.25
MF14	2+3	-7.61±0.03	-0.89±0.08	12.49±0.02	1.78±0.06	-9.46±0.02	-0.80±0.05
	2	-7.58±0.03	-1.29±0.19	12.50±0.02	1.64±0.13	-9.49±0.02	-0.52±0.11
MF15	2+3	-8.16±0.05	-0.59±0.11	10.40±0.03	1.30±0.07	-5.55±0.05	-0.45±0.12
	2	-8.15±0.05	-0.83±0.37	10.42±0.03	1.00±0.23	-5.57±0.05	0.10±0.39
MF16	2+3	-3.98±0.05	-0.23±0.08	36.68±0.03	3.04±0.05	5.14±0.03	0.75±0.05
	2	-3.93±0.09	-0.46±0.35	36.60±0.06	3.37±0.22	5.15±0.08	0.74±0.31
MF17	1+2+3	-11.41±0.03	-0.52±0.05	2.96±0.04	0.73±0.05	-1.48±0.05	-0.05±0.07
	2	-11.35±0.05	-0.82±0.25	2.97±0.06	0.51±0.28	-1.41±0.08	-0.53±0.36

^a Maser feature ID from Figure 4.

^b Each Cycle corresponds to the epochs: Cycle 1 (ϕ 1.00 ~ 1.25), Cycle 2 (ϕ 1.89 ~ 2.29), and Cycle 3 (ϕ 2.89 ~ 3.17).

^c The reference epoch is J2020.0 and the reference position is MF1. The fitted positions of MF1 with minor offsets are caused by the maser structures.

^d The radial velocity drift

^e The relative proper motions are defined as $\mu_x = \mu_\alpha \cos \delta$ and $\mu_y = \mu_\delta$.

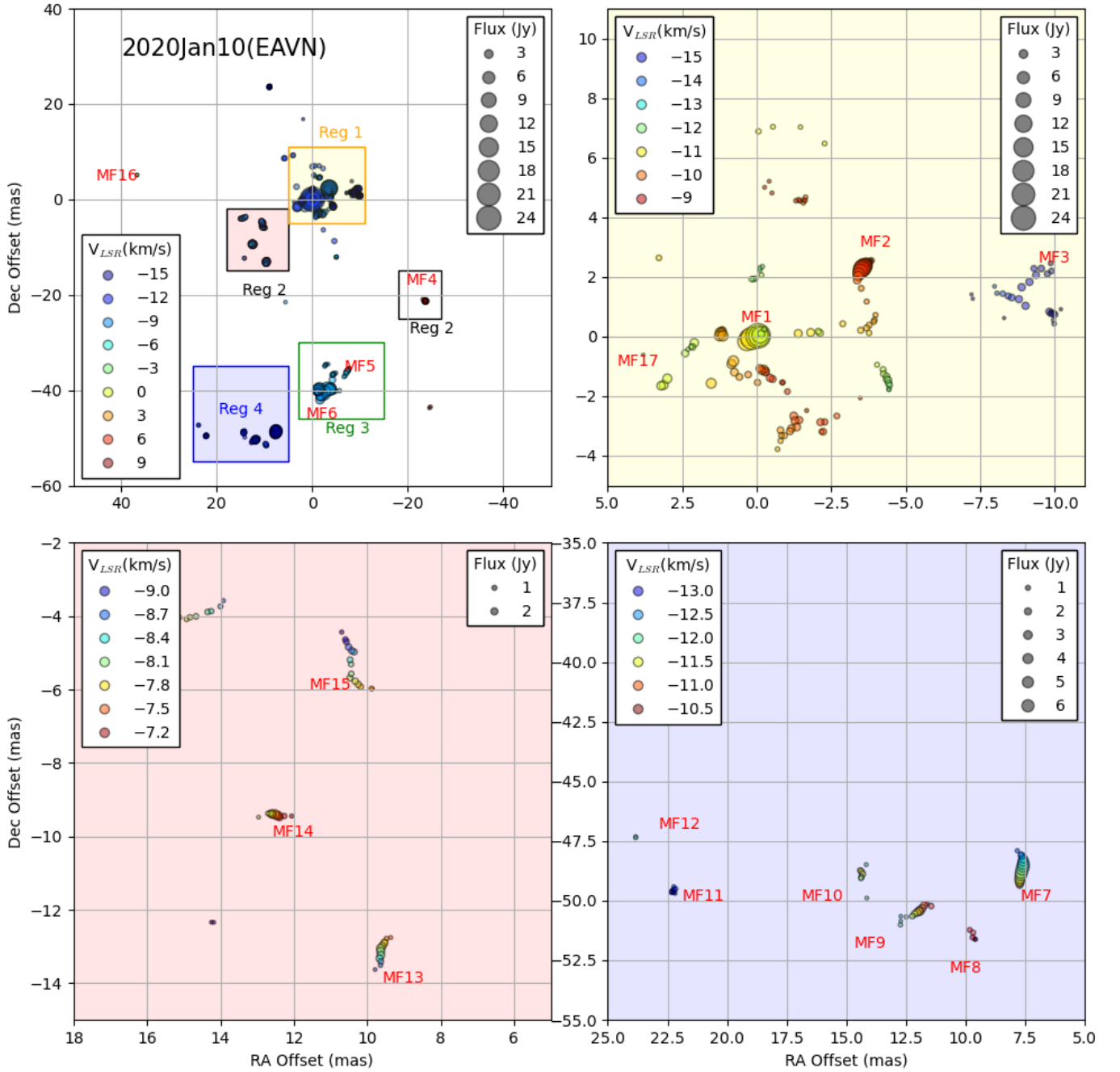


Figure 4. EAVN images of the spatial structures of maser features (top left), with a zoom-in of the colored blocks (top right, bottom left, bottom right), observed on 2020 Jan 10 (ϕ 2.00). These images are obtained after component fitting from the image data cube with AIPS task SAD. Each of the filled circles shows a velocity component (maser spot), and each maser feature (MF#) has a velocity channel spacing of 0.105 km s^{-1} . The position reference feature (MF1) is around the map origin.

3.3. Astrometry

3.3.1. VERA Bona-Fide Astrometry in ESTEMA

As marked in Table 1, 14 epochs of data yielded successful phase-referencing astrometry with VERA dual-beam system. The dual-beam astrometry failed at other epochs due to various reasons, such as the masers in the trough of

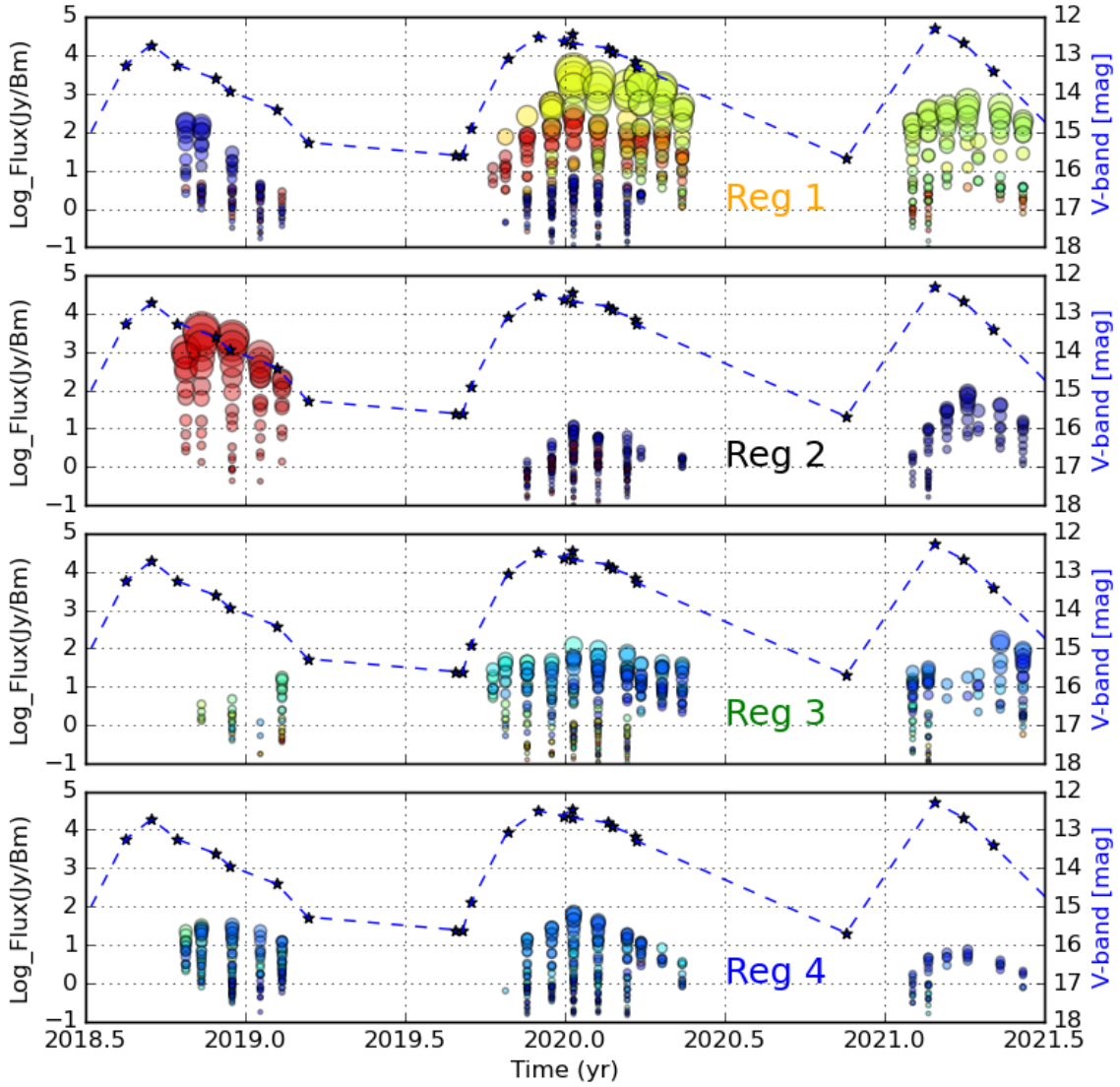


Figure 5. Temporal variation of maser features in different regions. The locations of the different regions are shown in Figure 4, while Region 1 includes MF[1,2,3,17], Region 2 includes MF[4,13,14,15], Region 3 includes MF[5,6], Region 4 includes MF[7,8,9,10,11,12]. The velocity gradient is classified by color and the size of maser spots means the flux density. The color and size of maser spots are the same to Fig 15. Optical light curve found in the AAVSO photometric data (blue stars).

the stellar pulsation cycles being too weak, key stations missing, and low sensitivity due to bad weather. The compact calibrator J0524+7034 shown in Figure 6 was used as the phase reference source, thus we expect no or little effects from its source structure.

As shown in Figure 3, few maser features can be detected with VERA alone. Among them, MF1 is the brightest maser feature, which can be detected over one year. The maser feature position can not be well determined using only one maser spot, because the maser spots are blended in position and frequency and the intensity of the blended components can vary with time (as shown in Figure 15). Instead, we used positions in about 5 spectral channels (velocity spacing of $\sim 0.5 \text{ km s}^{-1}$) where the maser spots were at the peak brightness, with compact emission and minimal blending. The positions of the maser spots relative to the calibrator J0524+7034 were measured as a function of time, and the positions were then modeled by the parallax, proper motion, position at a reference epoch, and the possible acceleration. We then assess the astrometric quality based on the magnitude of the post-fit residuals. The formal position uncertainties were usually smaller than the actual error, since the unknown systematic error (i.e., the

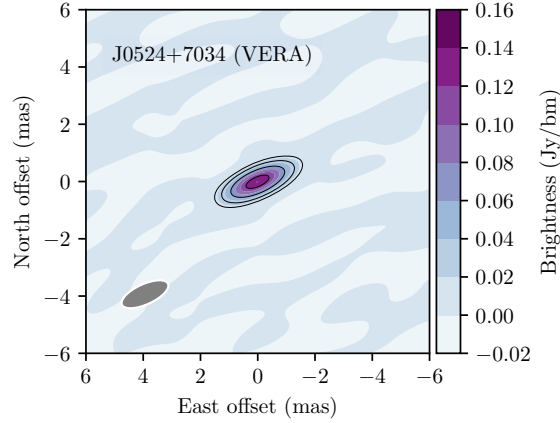


Figure 6. VERA image of J0524+7034 observed on 2020 January 10. The contour map is drawn with contour levels of 3,6,12,24,... $\times\sigma$, where 1σ corresponds to $0.005 \text{ Jy beam}^{-1}$.

tropospheric delay residual, maser structures, etc.) often dominate over random noise (Reid et al. 2009; Nagayama et al. 2020). The systematic error was added in quadrature to the priori error so that the reduced chi-square value became nearly unity.

Figure 7 and Table 3 show the outcomes of the astrometric fitting for MF1 positions measured with the VERA astrometric technique (Nagayama et al. 2020). In this astrometric fitting, we compared the different parameters, such as, using the data at different timescales and including the acceleration or not. We found different deviations from a common constant proper motion, or an acceleration, in declination between 2020 and 2021. This could come from either the variation in the maser structure (Figure 16) or a non-uniform acceleration in the maser feature. Taking into account the ambiguity in the results from these different estimation procedures, we conservatively obtained a parallax value of $1.79\pm 0.08 \text{ mas}$. This is consistent with $1.76\pm 0.10 \text{ mas}$ from *Gaia* EDR3 (Gaia Collaboration et al. 2021) and $1.73\pm 0.03 \text{ mas}$ from the previous VERA result (Matsuno et al. 2020) within 1 sigma level. The proper motions of the individual maser features usually are different from the central star, due to the extra internal motions of the masers. However, the proper motion of the maser feature MF1 ($14.37\pm 0.20, -35.46\pm 0.44 \text{ mas yr}^{-1}$) is consistent with *Gaia* EDR3 ($14.29\pm 0.07, -34.63\pm 0.10 \text{ mas yr}^{-1}$) within 1 sigma in east direction and 2 sigma in north direction, due to a small projection distance (less than 7 mas as discussed in Section 3.3.3) between MF1 and central star.

Table 3. Astrometric fitting for MF1 with VERA

MF ^a	Time	Acceleration	Parallax	μ_x ^b	μ_y ^b	Acc x ^c	Acc y ^c	RMS RA/Dec ^d
ID	Range	Estimation	(mas)	mas yr ⁻¹	mas yr ⁻¹	mas yr ⁻²	mas yr ⁻²	(mas mas)
MF1	2019.8-2021.3	No	1.90 ± 0.02	14.35 ± 0.02	-35.13 ± 0.02	-	-	0.082 0.060
	2019.8-2021.3	Yes	1.82 ± 0.03	14.08 ± 0.06	-35.51 ± 0.10	0.47 ± 0.10	0.70 ± 0.19	0.081 0.040
	2020.2-2021.3	No	1.75 ± 0.05	14.40 ± 0.04	-35.04 ± 0.03	-	-	0.093 0.043
	2020.2-2021.3	Yes	1.67 ± 0.07	14.65 ± 0.25	-36.15 ± 0.23	-0.36 ± 0.34	1.53 ± 0.32	0.093 0.027
Combined ^e			1.79 ± 0.08	14.37 ± 0.20	-35.46 ± 0.44			

^a Maser feature ID from Figure 4.

^b Absolute proper motions are defined as $\mu_x = \mu_\alpha \cos \delta$ and $\mu_y = \mu_\delta$.

^c The fitted accelerations/decelerations.

^d The root mean square (RMS) of the residuals in RA and Dec.

^e The unweighted average and standard deviation.

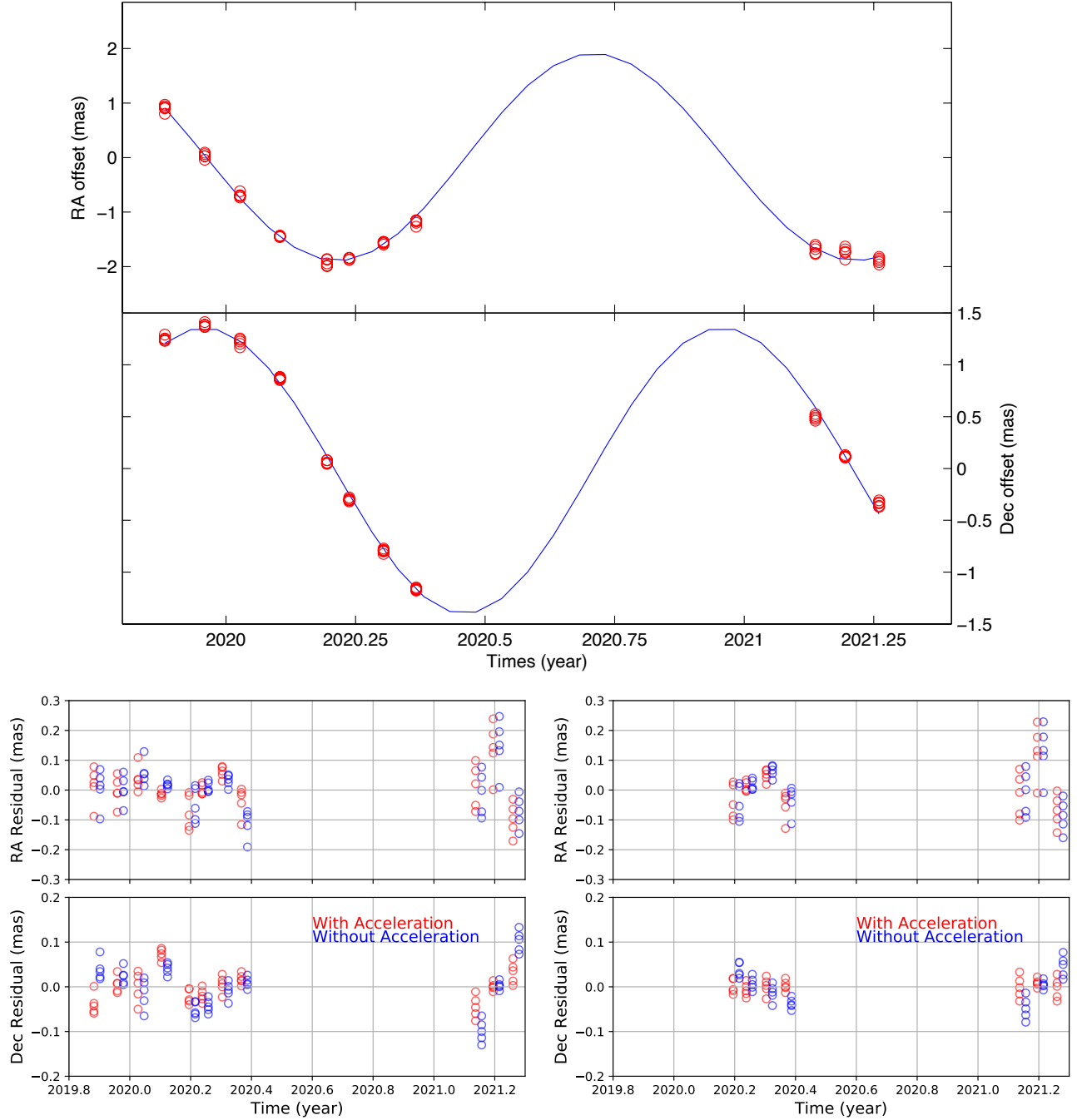


Figure 7. Parallax fitting for MF1 with VERA astrometry. Top panel: An example of the fitted parallax curve using the data points during the period 2019.8–2021.3 without an acceleration. Bottom-left panel: Residuals of the fitting using the data points during the period 2019.8–2021.3. The data points from the fitting including an acceleration have a constant horizontal offset from those without an acceleration for clarity. Bottom-right panel: Same as the bottom-left panel but the period 2020.2–2021.3.

3.3.2. Astrometric fitting for maser features with the EAVN data

We can obtain the absolute positions of the bright and compact maser spots from the 14 epochs with the VERA data. The bright and compact maser feature (MF1 in ϕ 1.89 ~ 2.29 and ϕ 2.93 ~ 3.03 , MF4 in ϕ 1.04 ~ 1.19) was then used to register the VERA and EAVN maps. The registration accuracy can be expressed as $\sigma_{registration} = \sqrt{\sigma_{thermalVERA}^2 + \sigma_{structureVERA}^2 + \sigma_{thermalEAVN}^2 + \sigma_{structureEAVN}^2}$, where $\sigma_{thermal}$ is the thermal (random) noise

determined by an elliptical Gaussian fitting with the AIPS task “SAD” and $\sigma_{structure}$ is the error effected by maser structure estimated by the blended peak components as shown in Figure 15 in the VERA/EAVN images. Because MF1 and MF4 are bright and compact, the thermal noises are < 0.02 mas and structure errors are ~ 0.05 mas for both VERA and EAVN maps. We believe the registration errors between VERA and EAVN maps are typically ~ 0.1 mas. These registration errors are used as the prior errors in the astrometric fitting. Note that this uncertainty may be propagated to the errors in deriving the parallaxes of maser features with the astrometrically registered EAVN maps, as described in Section 4.1.

Table 4 shows the independent parallax fits for the residuals of maser feature positions derived after subtracting the modulation of the annual parallax derived from the VERA data. The results were based on the same fitting procedures as mentioned in Section 3.3.1 and with/without acceleration parameters were compared. Averaging all the fitting results, we obtained a combined parallax residual of 0.07 ± 0.06 mas, which is consistent with the estimated error of the parallax ($\pi = 1.79 \pm 0.08$ mas).

3.3.3. The stellar position in the H₂O maser distribution

Determining the stellar position with respect to the H₂O maser distribution is important to estimate the center of 3-D kinematics. *Gaia* EDR3 provided the stellar position with optical astrometry, however there may exist uncertainty for this AGB star (Xu et al. 2019). On the other hand, the center of the SiO maser ring should correspond to the position of the star. Figure 8 shows the registered map of the H₂O and SiO masers with the KVN data, to which the SFPR calibration technique was applied (Dodson et al. 2014). The positional reference is the H₂O maser at $V_{LSR} = -11.05$ km s⁻¹ (MF1). We obtained the position of the central star (-5.1 ± 0.3 mas, -0.8 ± 0.2 mas) as indicated as the center of the solid circle in the least-squares circle method (Yoon et al. 2018). The estimated position of the central star is consistent with *Gaia* EDR3 result (-6.5 ± 0.3 mas, $+1.5 \pm 0.4$ mas) with an uncertainty of 2.7 mas on 2020 January 10. The differences between the estimated position and *Gaia* EDR3 result (-6.5 ± 0.3 mas, $+1.5 \pm 0.4$ mas) are 1.4 mas (~ 3 sigma) in east direction and 2.3 mas (~ 5 sigma) in north direction on 2020 January 10.

3.4. The expansion of the BX Cam flow traced by H₂O masers

Figure 9 displays the astrometric animation of H₂O masers at the 33 epochs from 2018 May 24 to 2021 Jun 9. Because of variable intervals of the observation epochs, including large blanks of the observations, the final version of the animation will be edited with some epoch-interpolation technique (Gonidakis et al. 2013). Even the current version of the animation, one can recognize radial outward motions of the H₂O maser features, helping us for noting interesting properties of the maser motions described as follows.

Figure 10 and 11 present the combined cube of the maser features synthesized with the cubes from the “High-Res. Imaging” in Table 1. The constant velocity proper motions and spoke-like maser features in BX Cam “point back” towards the central star. However, the point-back directions of the maser features in different groups (e.g, group MF[7,8,9,10,11,12] and group MF[13,14,15]) may converge into different areas, which may also have offsets from the location of the central star and the ring of SiO masers, as shown by auxiliary dashed lines. Thus the H₂O maser kinematics may have origins different from the central star, if we assume that masers have the constant proper motions.

The CSE of BX Cam were reported with the LSR velocity range from -5 to $+5$ km s⁻¹ for SiO masers (Matsuno et al. 2020), from -16 to -4 km s⁻¹ and from $+7$ to $+10$ km s⁻¹ for H₂O masers (Figure 12), from $+12$ to $+17$ km s⁻¹ for OH masers (Slootmaker et al. 1985), and up to 21 km s⁻¹ for CO $J = 1 \rightarrow 0$ line (Knapp & Morris 1985), which shows a gradual acceleration from SiO maser to CO $J = 1 \rightarrow 0$ line.

Figure 12 shows the angular distance–LSR velocity diagram of the H₂O maser features. To examine the variation of maser flows on long timescales, we compared the maser maps made by VERA from 2012 to 2014 (Matsuno et al. 2020) and made by ESTEMA from 2018 to 2021 (Figure 10). Figure 13 shows the registered map of the ESTEMA maser flows with that of Matsuno et al. (2020). Adopting a radial velocity of BX Cam as 0 km s⁻¹ (Matsuno et al. 2020), we derived the three dimensional expanding velocities of H₂O maser features using V_{LSR} and internal proper motions. The maser map of Matsuno et al. (2020) showed only the blueshift dominant features with respect to the central star. They obtained a three-dimensional velocity of 14.8 ± 1.4 km s⁻¹ with three collimated flows, and concluded that the H₂O masers trace an outflow with a quite uniform velocity. However, our result shows a wider range of 9 km s⁻¹ (inner radii) to 19 km s⁻¹ (outer radii) at different directions. These differences may be caused by the different observational epochs (different pulsation phases) originated from characteristics of the Mira variable star BX Cam, which traces the different expanding shells relative to Matsuno et al. (2020).

Table 4. Astrometric fitting for positions of the maser features with EAVN, registered using VERA astrometry

MF ^a	Time	Acceleration	Residual ^b	μ_x ^c	μ_y ^c	Acc x ^d	Acc y ^d	RMS RA/Dec ^e
ID	Range (Epochs)	Estimation	Parallax (mas)	mas yr ⁻¹	mas yr ⁻¹	mas yr ⁻²	mas yr ⁻²	(mas mas)
MF1	2019.8-2021.3 (11)	Yes	0.00±0.04	14.08±0.06	-35.51±0.10	0.47±0.10	0.70±0.19	0.081 0.040
		No	0.00±0.03	14.35±0.02	-35.13±0.02	-	-	0.082 0.060
MF2	2018.8-2021.3 (13)	Yes	0.13±0.04	14.40±0.02	-34.92±0.02	0.14±0.05	-0.48±0.05	0.075 0.094
		No	0.05±0.03	14.38±0.02	-34.85±0.03	-	-	0.083 0.161
MF3	2018.8-2021.2 (11)	Yes	0.06±0.09	14.79±0.51	-36.43±0.23	-0.28±0.28	-1.82±0.45	0.601 0.470
		No	0.11±0.06	14.62±0.08	-35.51±0.05	-	-	0.609 0.446
MF4	2018.8-2020.2 (8)	Yes	0.09±0.05	13.46±0.18	-35.77±0.20	0.73±0.26	0.09±0.32	0.059 0.104
		No	0.02±0.04	13.01±0.03	-35.84±0.07	-	-	0.057 0.103
MF5	2019.0-2021.2 (5)	Yes	0.07±0.11	13.56±0.12	-37.50±0.17	0.66±0.26	0.29±0.34	0.314 0.362
		No	0.02±0.09	13.85±0.17	-37.34±0.11	-	-	0.354 0.360
MF7	2018.9-2021.3 (13)	Yes	0.17±0.07	14.81±0.17	-38.22±0.22	0.35±0.29	-0.62±0.40	0.078 0.189
		No	0.09±0.04	14.99±0.04	-38.51±0.05	-	-	0.082 0.192
MF8	2018.8-2021.2 (9)	Yes	0.12±0.09	15.78±0.05	-39.65±0.04	0.14±0.11	-0.04±0.14	0.179 0.141
		No	0.08±0.05	15.78±0.05	-39.64±0.03	-	-	0.180 0.141
MF9	2018.8-2021.2 (12)	Yes	0.05±0.06	15.32±0.05	-38.70±0.05	-0.17±0.09	0.03±0.11	0.294 0.172
		No	-0.01±0.04	15.37±0.04	-38.70±0.03	-	-	0.298 0.172
MF10	2019.8-2021.3 (10)	Yes	0.17±0.09	15.65±0.26	-38.28±0.24	0.16±0.47	-0.58±0.48	0.139 0.198
		No	0.11±0.06	15.59±0.07	-38.02±0.08	-	-	0.139 0.200
MF11	2018.8-2021.3 (7)	Yes	0.14±0.09	16.59±0.29	-38.87±0.27	-0.97±0.65	0.74±0.52	0.115 0.116
		No	0.11±0.05	17.06±0.05	-39.21±0.07	-	-	0.127 0.129
MF12	2018.8-2020.2 (4)	Yes	0.03±0.05	17.96±0.37	-38.95±0.48	0.86±0.47	-0.15±0.62	0.120 0.182
		No	0.04±0.05	17.48±0.18	-39.00±0.10	-	-	0.121 0.184
MF13	2018.8-2020.0 (10)	Yes	0.05±0.04	15.75±0.07	-36.26±0.15	-0.32±0.12	0.90±0.28	0.169 0.228
		No	0.01±0.03	15.60±0.01	-35.76±0.02	-	-	0.169 0.235
MF14	2019.9-2021.2 (9)	Yes	0.20±0.07	15.86±0.21	-35.23±0.28	0.52±0.37	-1.35±0.50	0.169 0.101
		No	0.05±0.04	16.04±0.08	-35.95±0.08	-	-	0.184 0.130
MF15	2019.8-2021.2 (7)	Yes	0.11±0.12	14.90±0.42	-34.94±0.32	1.28±0.65	-1.21±0.55	0.208 0.308
		No	0.13±0.06	15.71±0.08	-35.60±0.10	-	-	0.210 0.314
MF16	2020.1-2021.2 (4)	Yes	0.07±0.14	16.76±0.41	-34.57±0.46	1.03±0.60	0.19±0.81	0.070 0.070
		No	0.00±0.09	17.46±0.10	-34.44±0.11	-	-	0.070 0.068
MF17	2019.0-2021.3 (12)	Yes	0.06±0.07	14.75±0.08	-35.16±0.11	0.46±0.14	-0.09±0.19	0.233 0.322
		No	-0.02±0.05	15.03±0.05	-35.18±0.07	-	-	0.250 0.321
	Combined ^f	Yes	0.10±0.05					
	Combined ^f	No	0.05±0.05					
	Combined ^f	ALL	0.07±0.06					

^a Maser feature ID from Figure 4.

^b The residual parallax after subtracting the parallax 1.82 ± 0.03 mas for with acceleration(Yes) and 1.90 ± 0.02 mas for without acceleration(No).

^c The relative proper motions are defined as $\mu_x = \mu_\alpha \cos \delta$ and $\mu_y = \mu_\delta$.

^d The possible accelerations/decelerations.

^e The root mean square (RMS) of the residuals in RA and Dec.

^f The unweighted average and standard deviation.

Base on Figure 9–13, there are three main groups of H₂O maser features. The first one (Group A: MF[1,2,3,13,14,15,17]) is associated with the inner blue-shifted maser feature closer to the central star, the second (Group B: MF[5,6,7,8,9,10,11,12]) is associated with the outer blue-shifted lobe of the outflow, and the third (Group C: MF4) is associated with the red-shifted maser feature of the outflow. The red-shifted maser feature of the outflow (from behind the central star) is very time variable as shown in Figure 1. The three-dimensional velocities are estimated to be 12.8 ± 3.5 km s⁻¹ for all maser features, 10.5 ± 2.0 km s⁻¹ for Group A, 15.5 ± 2.8 km s⁻¹ for Group B, and 10.1 km s⁻¹ for Group C (MF4).

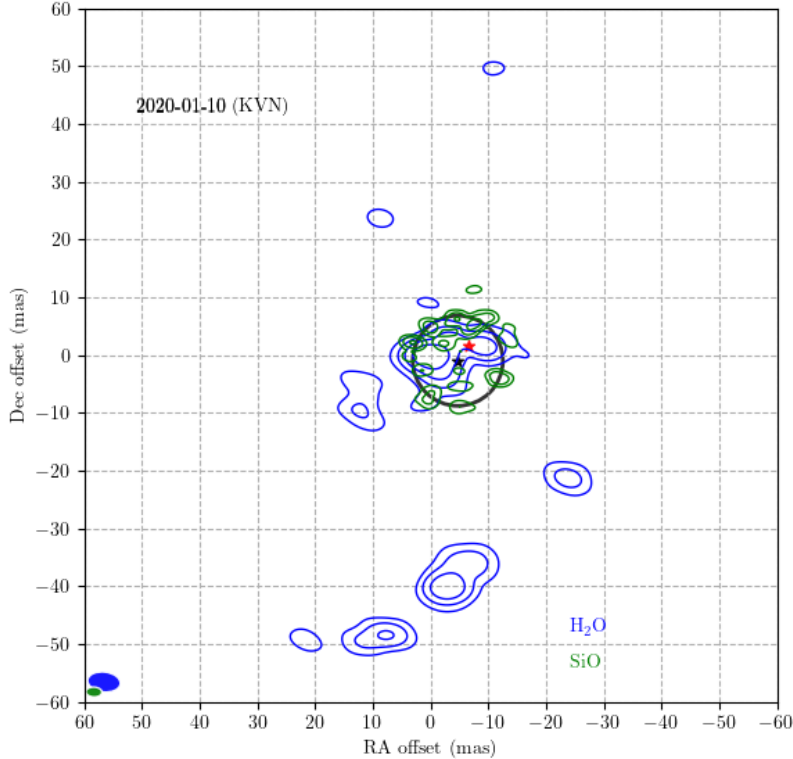


Figure 8. Registered map of the H₂O and SiO($v=1, J=1\rightarrow 0$) masers observed on 2020 January 10 using the KVN data, which were taken from velocity-channel integration with weights based on the root-mean-square noise level. Black star indicates the estimated position of the star at the center of the SiO maser ring using the least-squares circle method (Yoon et al. 2018). Red star indicates the position of the star derived from *Gaia* EDR3. The contour map is drawn with contour levels of 3,6,12,24,... $\times\sigma$, where 1σ corresponds to $0.025 \text{ Jy beam}^{-1}$ (H₂O) and $0.120 \text{ Jy beam}^{-1}$ (SiO), respectively.

We also made a least-squares model-fitting analysis assuming a model of an outflow that is radially expanding at a constant velocity. The detail of the modeling has already been described in Zhang et al. (2012). We adopted weights proportional to the square of the accuracy of a measured proper motion. The expansion center was assumed to be at the ring center of the SiO masers whose map registration was yielded in KVN SFPR (Section 3.3). The systemic velocity is adopted to be $\sim 0 \text{ km s}^{-1}$ (Matsuno et al. 2020). Thus the expansion velocity of H₂O masers is estimated to be $13.0 \pm 3.7 \text{ km s}^{-1}$, which is consistent with the result ($14.8 \pm 1.4 \text{ km s}^{-1}$) that found in the VERA observations during 2012–2014 (Matsuno et al. 2020). Figure 14 shows the spatial distribution and velocity vectors of the maser features with respect to the outflow origin projected on the R.A.-Distance (XZ) and Distance-Dec (ZY) planes, which was obtained after the model fit assuming a radially expanding flow (Imai et al. 2000). The outer masers roughly exhibit radial expansions and are located at similar distances from the central star at roughly a constant expansion velocity. Thus the masers seem to be associated with a spherically expanding outflow although the directions of the maser excitation are significantly biased and changed from time to time on the timescale of several years. However, there exist some big deviations from the spherical flow for the inner masers projected closely to the central star in the sky, which may be caused by the result of enhancement of large uncertainties in the maser positions on Z-axis and some random maser motions in the modeling.

4. DISCUSSION

4.1. Astrometry for CSE H₂O masers

Our work has evaluated the accuracy of the annual parallax measurement with CSE H₂O masers, majority of whom are located in the stellar neighborhood and exhibit extended brightness distributions. The importance of astrometry is also demonstrated for the maser animation, which is a key to register the maser images at different epochs and extract the intrinsic motions of maser features associated with the CSE.

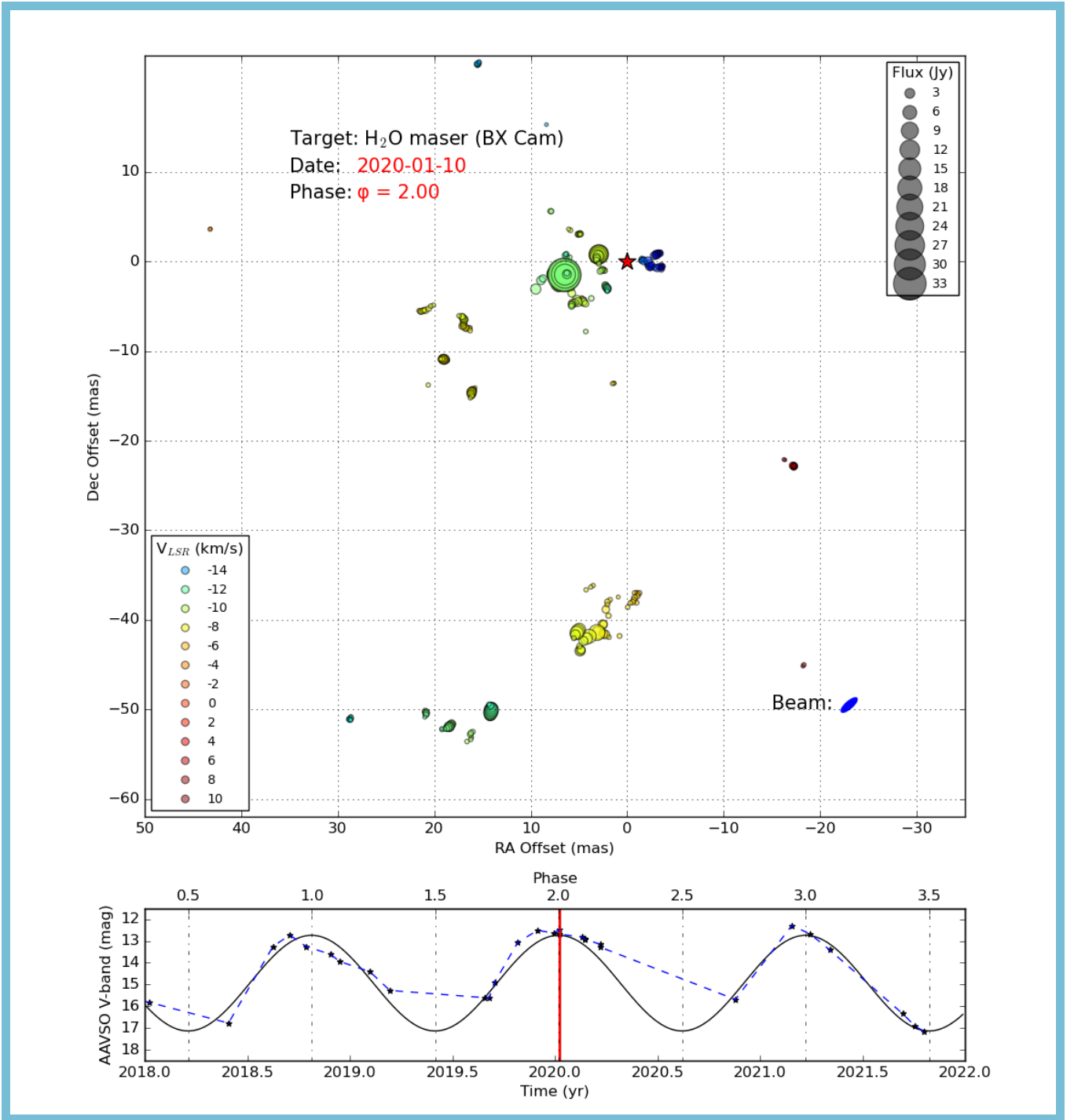


Figure 9. Astrometric Animation of H₂O masers around BX Cam. The coordinate system is astrometrically fixed with the star whose position is determined using *Gaia* EDR3. Maser feature motions on the sky with modulation due to the annual parallax (1.79 ± 0.08 mas) and the proper motion (14.37 ± 0.20 , -35.46 ± 0.44 mas yr⁻¹) of the referenced maser feature MF1 subtracted. A red-filled circle denotes the central star whose position (parallax: 1.76 ± 0.10 mas, proper motion: 14.29 ± 0.07 , -34.63 ± 0.10 mas yr⁻¹) has been determined in *Gaia* EDR3. The lower panel is the optical light curve of AAVSO and the red vertical line follows the phase. An animated version of this figure is available. It covers 33-epoch maser maps from 2018 May 24 to 2021 Jun 7. The video duration is 16 seconds.

The astrometric accuracy of the VERA was evaluated in detail by Nagayama et al. (2020), which achieves the parallax accuracy of $10 \mu\text{as}$ in the best cases. Our targets were observed with a background calibrator 2° away, and

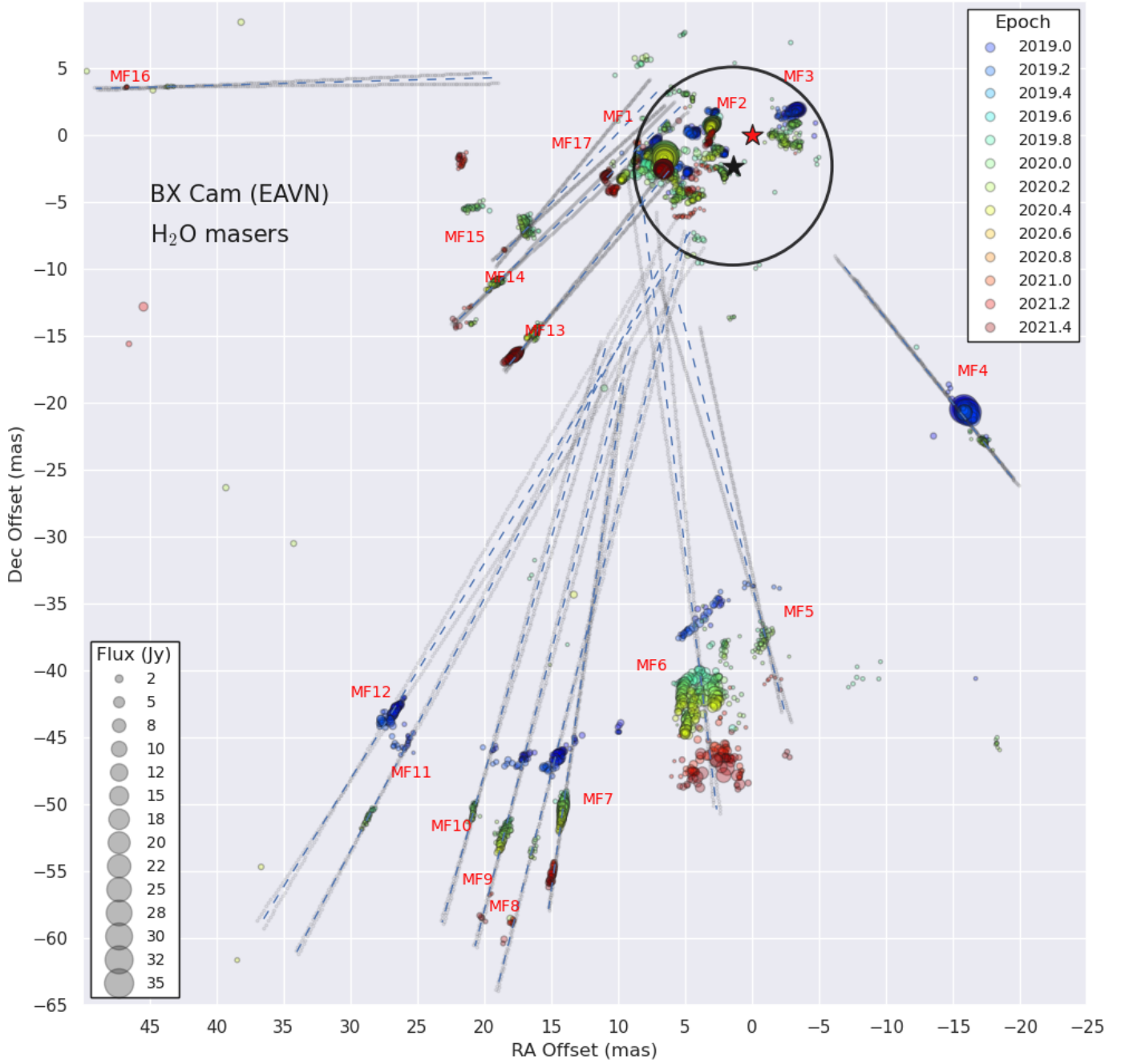


Figure 10. Expansion of the BX Cam flow traced by H₂O masers. The positional reference is *Gaia* EDR3 (red star). Black circle denotes the fitted ring of SiO masers in Section 3.3.3. The different colors of the maser spots indicate different observation epochs, which are astrometrically fixed using the method in Figure 9. An auxiliary dashed line indicates a possible trajectory of an maser feature from 2012 to 2022 at a constant velocity vector, while the nearby lines in light grey show the position error of the back-extrapolated motion vectors. The lines of motion are drawn with the positions and proper motions of the maser feathers estimated in Table 2.

at elevations of $\sim 50^\circ$. The single-epoch position accuracy for a given baseline can be estimated to be $\sim 80 \mu\text{s}$ using the Table 1 of Nagayama et al. (2020), indicating an expected parallax uncertainty better than $30 \mu\text{s}$ with 10 epochs extended over more than one year. However, our derived parallax ($1.79 \pm 0.08 \text{ mas}$) has an uncertainty more than twice

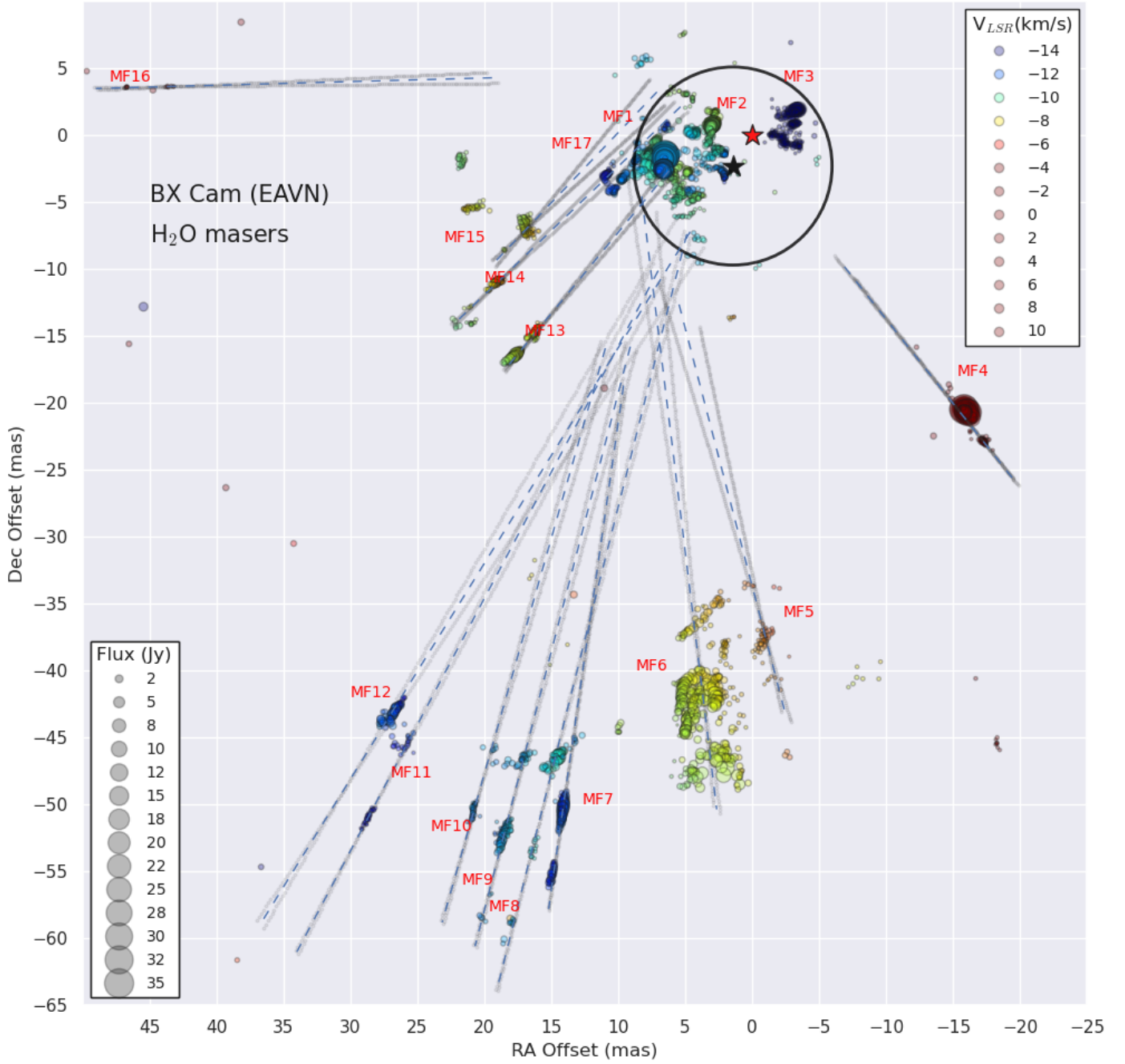


Figure 11. Same as Figure 10 but the different colors of the maser spots indicate different LSR velocities.

the expected one, probably due to the variation in the maser structure (MF1 in Figure 16) or an irregular motion due to shocks or radiation-coupled flow as shown in the Figure 7. Nevertheless it is consistent with that previously derived with VERA (1.73 ± 0.03 mas) (Matsuno et al. 2020) and *Gaia* EDR3 (1.76 ± 0.10 mas) (Gaia Collaboration et al. 2021) within 1 sigma. These parallaxes also rule out a larger parallax (4.13 ± 0.25 mas) reported in *Gaia* DR2 (Gaia Collaboration et al. 2018). There is evidence that there may exist uncertainty in the *Gaia* DR2 parallaxes for the AGB stars from their large sizes, temporal and spatial variation in the surface brightness, and/or extinction by the circumstellar dust (Xu et al. 2019). These factors may prevent the improvement of the parallax accuracy even in future *Gaia* results using more measurements and better calibration of systematics.

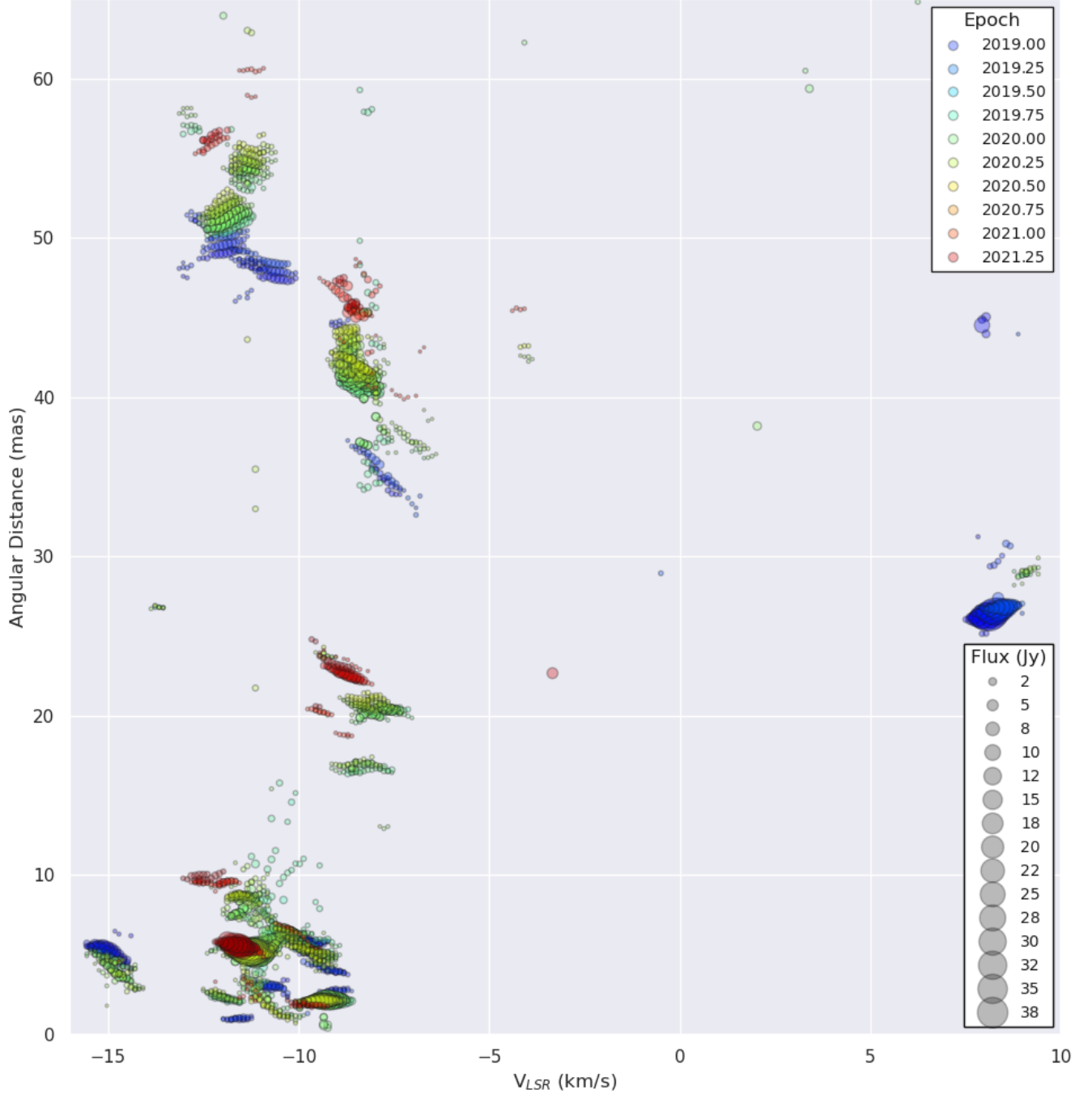


Figure 12. Angular distance–LSR velocity diagram. The position of the star was used as the center of the SiO maser ring.

As already shown in Section 3.3, the individual maser features also exhibit some deviations from linear motions. The smaller residuals in Figure 7 support the parallax fitting including such an acceleration. However, it is obscure whether the observed acceleration really reflects a real one rather than just an illusion caused by a drift of a maser emission area in the maser gas clump. This should be tested with further analysis of the observed accelerations in the combined maser features around this star. The residual parallaxes of all maser features found in the EAVN maps are probably affected by their extended structures, the errors in the astrometric registration of the EAVN and VERA maps, and/or the possible non-linear motions. Note that an additional error contribution as mentioned above may

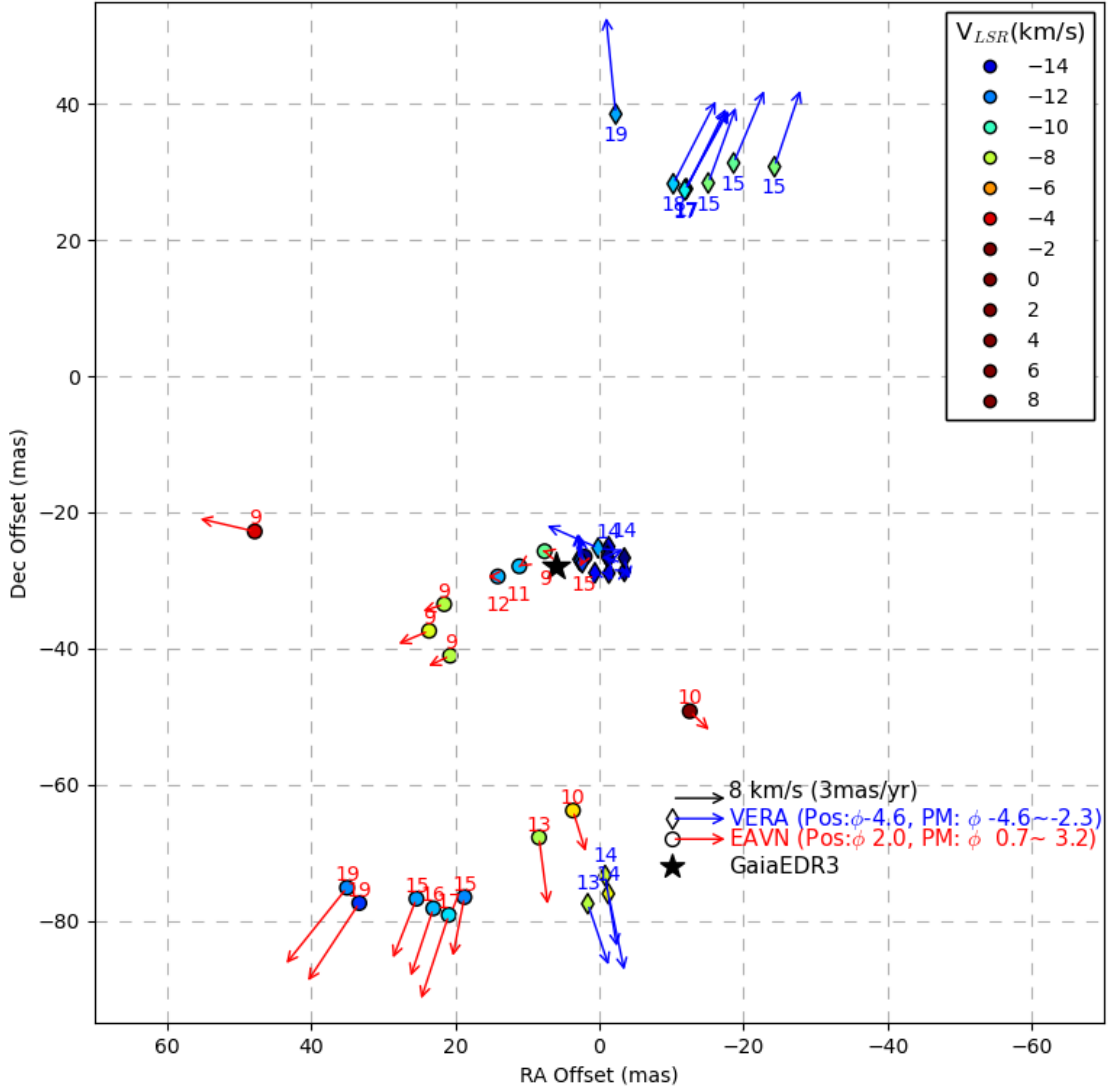


Figure 13. The registered maser flows from EAVN (ESTEMA) and VERA (Table 4 of Matsuno et al. 2020) observed at different pulsation circles. The registration is performed with *Gaia* EDR3. The numbers around the maser features are the three-dimensional velocities in km s^{-1} .

have possibilities to increase and decrease the parallax value. Therefore, we adopted a parallax value using MF1 only (Section 3.3.1) and give a conservative uncertainty that would cover all of the possible errors (Section 3.3.2).

The stellar position in the H_2O maser distribution was estimated to be at the ring center of the SiO masers whose locations are determined in the KVN astrometry with the SFPR technique at a single epoch. The SiO maser ring structure will be further clarified with multiple maser lines (Yoon et al. 2018). Even the present results, one can clearly see an offset of the expansion center of the H_2O maser flow from the center of the SiO maser ring as shown in Figure 10. This may be caused by either the uncertainty of the stellar proper motion measured in *Gaia* EDR3 and adopted in the maser map registration, or a possible deviation of the outflow from a radial expansion.

4.2. CSE spatio-kinematics: asymmetric maser distribution and its evolution

The asymmetry/inhomogeneity of the spatial distribution is evident throughout the three-dimensional maser kinematics of H_2O masers that we have revealed. The maser outflows are dominated by the blue-shifted H_2O maser features (dominant blue-shifted outflow of bipolar outflow). Compared to the maser features detected with VERA

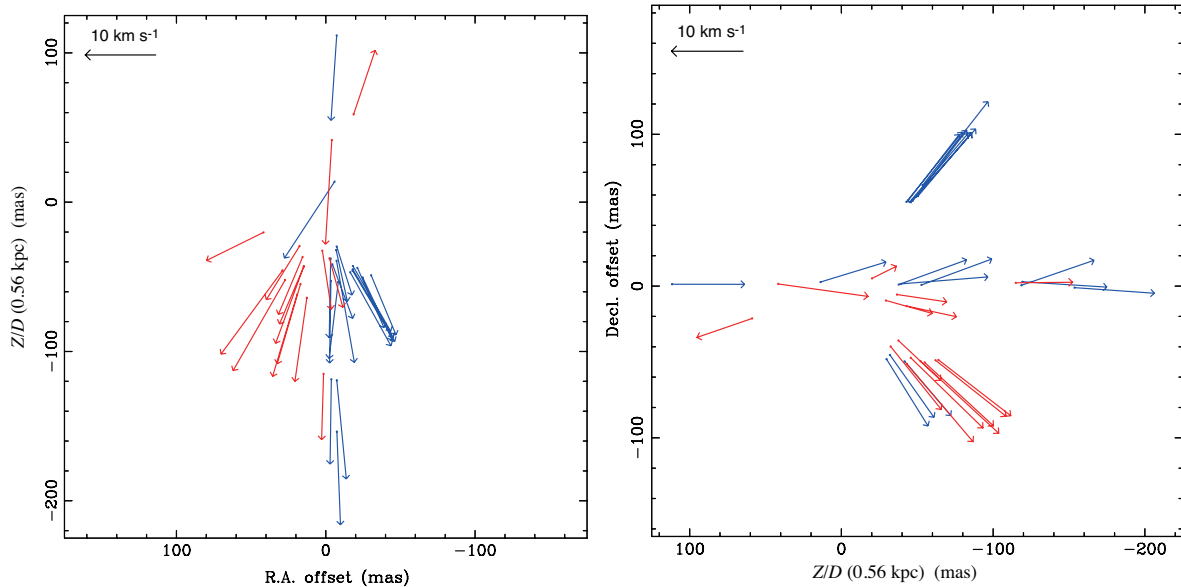


Figure 14. The Top view (Left panel: R.A.-Distance, XZ-plane) and the East-side view (Right panel: Distance-Dec., ZY-plane) of the estimated positions and proper motions with respect to the outflow origin, using the method of Imai et al. (2000). The base of the arrow is pointed to the position of the maser feature. The direction and length of the arrow represent the direction and magnitude of the proper motion, respectively. The red and blue arrows show the maser feature motions found in the EAVN (ESTEMA) and VERA observations (Matsuno et al. 2020), respectively.

from 2012 to 2014 (Matsuno et al. 2020), we have detected the central and southern components, and also new redshifted components. The northern components previously mapped by Matsuno et al. (2020) have become so faint that they are detected only on KVN baselines, at a few epochs.

Although the velocity field of the masers is generally consistent with the expanding shell model, the expansion is not strictly isotropic. For BX Cam, the distribution of the maser features is limited in a thick-shell region (Section 3.4), which has inner and outer expansion velocities of 9 km s^{-1} and 19 km s^{-1} at radii of $<20 \text{ mas}$ and 60 mas , respectively. There also exist gradual drifts in radial velocities and possible accelerations/decelerations in the proper motion. Here, we suppose a constant/gradual radial acceleration in a CSE (e.g. Richards 2012) for BX Cam. Adopting the distance to the star $D = 560 \text{ pc}$, one can calculate a travel time from the inner and outer radii of the expanding maser shell to be $t_{\text{travel}} \simeq 7.6 \text{ yr}$ and an acceleration to be $a \simeq 1.3 \text{ km s}^{-1} \text{ yr}^{-1}$, corresponding to $\dot{\mu} \simeq 0.5 \text{ mas yr}^{-2}$. This suggests that observed drifts of LSR velocities can be explained by this kind of acceleration while the accelerations/decelerations seen in the maser proper motions (up to 1.8 mas yr^{-2}) cannot. Because the accuracy of the observed accelerations/deceleration is currently insufficient for further astrophysical interpretation, we reserve further statistical analysis for a separate paper. Nevertheless, the existence of such accelerations or deviations from constant velocity motion, may be detectable in the systematic residuals after the parallax and proper motion fitting.

The expansion velocity and the projected distance to the central star of a mass-losing flow are seem to be time-dependent. The flows found in the ESTEMA data were compared with that in the VERA observations from 2012 to 2014 in Figure 13. Different shells and distributions were detected at different times and with different arrays.

Temporal variation in the morphology of individual maser features is also determined. The shapes of the maser structures are generally correlated with the direction of expansion. Figure 16 also shows the complex variation of the interior structure, such as interior rotation, expansion, sub-structure, and change of direction. This might be due to any or all of: bulk rotation, internal turbulence, or a pattern speed due to shock wave propagation (Richards et al. 2012, 2020).

4.3. Variability of the H₂O maser

A correlation between the 22 GHz H₂O maser and optical light curves with a time lag has been reported in AGB stars (Benson et al. 1993). BX cam is in also such a case, and the measured time lag between the integrated water maser and optical light curves is about $\sim 25 \text{ d}$. However, several bright masers often dominate the total integrated

intensity, and thus it is hard to depict the variation of individual maser features or spots without spatially resolved maser maps. Our VLBI images allow us to trace individual maser features (shown in Figure 15) and groups of maser features (shown in Figure 5). We find that the light curves of the individual maser features or groups have different time lags with the optical light curve. We note that H₂O masers are pumped by collision rather than radiation field, and hence other factors should be considered to interpret the correlation between maser and optical light curves, such as shock waves caused by stellar pulsation or giant planets, revolving the central star (Struck-Marcell 1988; Rybicki & Denis 2001; Richards et al. 2012).

5. SUMMARY

We have measured the trigonometric parallaxes, proper motions, drifts in LSR velocities, and the possible accelerations/decelerations of the H₂O masers around the Mira variable BX Cam using EAVN observations. Our parallax is 1.79 ± 0.08 mas, which is consistent with *Gaia* EDR3 and previously measured VLBI parallaxes within their joint uncertainties. The stellar position with respect to the H₂O masers is registered by a ring of SiO masers using the KVN SFPR astrometry, which is consistent with that of *Gaia* EDR3 within 3 mas. There are asymmetries/inhomogeneities in both the spatial and velocity distributions of the H₂O masers although their motions are roughly modeled with a spherically expanding outflow. In fact, the maser locations have been dominant in a blue-shifted outflow with respect to the central star. The 3D H₂O maser kinematics indicates that the circumstellar envelope is expanding at a velocity of 13 ± 4 km s⁻¹. A time lag of about 25 d is also measured between the integrated water maser and optical light curves. More detailed maser kinematics for the CSE around BX Cam will appear in separate papers, covering multiple maser-line movies with SiO masers and the further discussion on the possibility of the maser clump acceleration.

ACKNOWLEDGMENTS

We acknowledge with thanks the variable star observations from the AAVSO International Database contributed by observers worldwide and used in this research. We are grateful to all staff members in EAVN who helped to operate the array and to correlate the data. Particularly, the interferometer model (IM) files are provided by Mr. DongKyu Jung, and the delay re-calculation tables are made by Dr. Takumi Nagayama and Dr. Kazuya Hachisuka. The KVN is a facility operated by Korea Astronomy and Space Science Institute (KASI) and VERA is a facility operated by the National Astronomical Observatory of Japan (NAOJ) in collaboration with associated universities in Japan. Tianma 65-m telescope is operated by Shanghai Astronomical Observatory (SHAO). Nanshan 26-m telescope is operated by Xinjiang Astronomical Observatory (XAO). Takahagi 32-m telescope is operated by NAOJ and Ibaraki University and partially supported by the Inter-university collaborative project “Japanese VLBI Network (JVN)” of NAOJ. HI and MO was supported by JSPS KAKENHI JP16H02167. LC is supported by the CAS “Light of West China” Program (Grant No. 2021-XBQNXZ-005) and the National Natural Science Foundation of China (Grant No. U2031212). AMS was supported by the Russian Ministry of Science and Higher Education, No. FEUZ-2020-0030. BZ was supported by the National Natural Science Foundation of China (Grant No. U2031212 and U1831136), and Shanghai Astronomical Observatory, Chinese Academy of Sciences (Grant No. N2020-06-19-005).

Facilities: EAVN

Software: AIPS (Greisen 2003), ParselTongue (Kettenis et al. 2006), Astropy (Astropy Collaboration et al. 2013)

REFERENCES

- Astropy Collaboration, Robitaille, T. P., Tollerud, E. J., et al. 2013, *A&A*, 558, A33, doi: [10.1051/0004-6361/201322068](https://doi.org/10.1051/0004-6361/201322068)
- Benn, D. 2012, *JAAVSO*, 40, 852
- Benson, P. J., Little-Marelin, I. R., & Cadmus, Robert R., J. 1993, in *Astrophysical Masers*, ed. A. W. Clegg & G. E. Nedoluha, Vol. 412, 271–274, doi: [10.1007/3-540-56343-1_259](https://doi.org/10.1007/3-540-56343-1_259)
- Cho, I., Jung, T., Zhao, G.-Y., et al. 2017, *PASJ*, 69, 87, doi: [10.1093/pasj/psx090](https://doi.org/10.1093/pasj/psx090)

- Diamond, P. J., & Kemball, A. J. 2003, *ApJ*, 599, 1372, doi: [10.1086/379347](https://doi.org/10.1086/379347)
- Diamond, P. J., Kemball, A. J., Junor, W., et al. 1994, *ApJ*, 430, L61, doi: [10.1086/187438](https://doi.org/10.1086/187438)
- Dodson, R., Rioja, M. J., Jung, T.-H., et al. 2014, *AJ*, 148, 97, doi: [10.1088/0004-6256/148/5/97](https://doi.org/10.1088/0004-6256/148/5/97)
- Engels, D., Schmid-Burgk, J., & Walmsley, C. M. 1988, *A&A*, 191, 283
- Gaia Collaboration, Brown, A. G. A., Vallenari, A., et al. 2018, *A&A*, 616, A1, doi: [10.1051/0004-6361/201833051](https://doi.org/10.1051/0004-6361/201833051)
- . 2021, *A&A*, 649, A1, doi: [10.1051/0004-6361/202039657](https://doi.org/10.1051/0004-6361/202039657)
- Gonidakis, I., Diamond, P. J., & Kemball, A. J. 2010, *MNRAS*, 406, 395, doi: [10.1111/j.1365-2966.2010.16716.x](https://doi.org/10.1111/j.1365-2966.2010.16716.x)
- . 2013, *MNRAS*, 433, 3133, doi: [10.1093/mnras/stt954](https://doi.org/10.1093/mnras/stt954)
- Greisen, E. W. 2003, in *Astrophysics and Space Science Library*, Vol. 285, *Information Handling in Astronomy - Historical Vistas*, ed. A. Heck, 109, doi: [10.1007/0-306-48080-8_7](https://doi.org/10.1007/0-306-48080-8_7)
- Habing, H. J. 1996, *A&ARv*, 7, 97, doi: [10.1007/PL00013287](https://doi.org/10.1007/PL00013287)
- Habing, H. J., & Olofsson, H. 2004, *Asymptotic Giant Branch Stars*, doi: [10.1007/978-1-4757-3876-6](https://doi.org/10.1007/978-1-4757-3876-6)
- Höfner, S. 2011, in *Astronomical Society of the Pacific Conference Series*, Vol. 445, *Why Galaxies Care about AGB Stars II: Shining Examples and Common Inhabitants*, ed. F. Kerschbaum, T. Lebzelter, & R. F. Wing, 193. <https://arxiv.org/abs/1102.5268>
- Höfner, S., Bladh, S., Aringer, B., & Ahuja, R. 2016, *A&A*, 594, A108, doi: [10.1051/0004-6361/201628424](https://doi.org/10.1051/0004-6361/201628424)
- Höfner, S., & Olofsson, H. 2018, *A&ARv*, 26, 1, doi: [10.1007/s00159-017-0106-5](https://doi.org/10.1007/s00159-017-0106-5)
- Honma, M., Yoon, K. C., Bushimata, T., et al. 2004, *PASJ*, 56, L15, doi: [10.1093/pasj/56.3.L15](https://doi.org/10.1093/pasj/56.3.L15)
- Honma, M., Kijima, M., Suda, H., et al. 2008, *PASJ*, 60, 935, doi: [10.1093/pasj/60.5.935](https://doi.org/10.1093/pasj/60.5.935)
- Imai, H., Kameya, O., Sasao, T., et al. 2000, *ApJ*, 538, 751, doi: [10.1086/309165](https://doi.org/10.1086/309165)
- Imai, H., Shibata, K. M., Marvel, K. B., et al. 2003, *ApJ*, 590, 460, doi: [10.1086/374887](https://doi.org/10.1086/374887)
- Kettenis, M., van Langevelde, H. J., Reynolds, C., & Cotton, B. 2006, in *Astronomical Society of the Pacific Conference Series*, Vol. 351, *Astronomical Data Analysis Software and Systems XV*, ed. C. Gabriel, C. Arviset, D. Ponz, & S. Enrique, 497
- Khoury, T., Vlemmings, W. H. T., Paladini, C., et al. 2020, *A&A*, 635, A200, doi: [10.1051/0004-6361/201834618](https://doi.org/10.1051/0004-6361/201834618)
- Kim, J., Cho, S.-H., & Kim, S. J. 2014, *AJ*, 147, 22, doi: [10.1088/0004-6256/147/1/22](https://doi.org/10.1088/0004-6256/147/1/22)
- Knapp, G. R., & Morris, M. 1985, *ApJ*, 292, 640, doi: [10.1086/163197](https://doi.org/10.1086/163197)
- Lebzelter, T., Mowlavi, N., Lecoœur-Taibi, I., et al. 2022, arXiv e-prints, arXiv:2206.05745. <https://arxiv.org/abs/2206.05745>
- Lee, S.-S., Oh, C. S., Roh, D.-G., et al. 2015, *Journal of Korean Astronomical Society*, 48, 125, doi: [10.5303/JKAS.2015.48.2.125](https://doi.org/10.5303/JKAS.2015.48.2.125)
- Lomb, N. R. 1976, *Astrophysics and Space Science*, 39, 447, doi: [10.1007/BF00648343](https://doi.org/10.1007/BF00648343)
- Matsuno, M., Nakagawa, A., Morita, A., et al. 2020, *PASJ*, 72, 56, doi: [10.1093/pasj/psaa022](https://doi.org/10.1093/pasj/psaa022)
- Nagayama, T., Kobayashi, H., Hirota, T., et al. 2020, *PASJ*, 72, 52, doi: [10.1093/pasj/psaa034](https://doi.org/10.1093/pasj/psaa034)
- Reid, M. J. 1999, in *Astronomical Society of the Pacific Conference Series*, Vol. 180, *Synthesis Imaging in Radio Astronomy II*, ed. G. B. Taylor, C. L. Carilli, & R. A. Perley, 481
- Reid, M. J., Menten, K. M., Brunthaler, A., et al. 2009, *ApJ*, 693, 397, doi: [10.1088/0004-637X/693/1/397](https://doi.org/10.1088/0004-637X/693/1/397)
- Richards, A. M. S. 2012, in *Cosmic Masers - from OH to H0*, ed. R. S. Booth, W. H. T. Vlemmings, & E. M. L. Humphreys, Vol. 287, 199–208, doi: [10.1017/S1743921312006977](https://doi.org/10.1017/S1743921312006977)
- Richards, A. M. S., Etoke, S., Gray, M. D., et al. 2012, *A&A*, 546, A16, doi: [10.1051/0004-6361/201219514](https://doi.org/10.1051/0004-6361/201219514)
- Richards, A. M. S., Sobolev, A., Baudry, A., et al. 2020, *Advances in Space Research*, 65, 780, doi: [10.1016/j.asr.2019.05.052](https://doi.org/10.1016/j.asr.2019.05.052)
- Rybicki, K. R., & Denis, C. 2001, *Icarus*, 151, 130, doi: [10.1006/icar.2001.6591](https://doi.org/10.1006/icar.2001.6591)
- Scargle, J. D. 1982, *ApJ*, 263, 835, doi: [10.1086/160554](https://doi.org/10.1086/160554)
- Shintani, M., Imai, H., Ando, K., et al. 2008, *PASJ*, 60, 1077, doi: [10.1093/pasj/60.5.1077](https://doi.org/10.1093/pasj/60.5.1077)
- Slootmaker, A., Habing, H. J., & Herman, J. 1985, *A&AS*, 59, 465
- Solf, J. 1978, *A&AS*, 34, 409
- Struck-Marcell, C. 1988, *ApJ*, 330, 986, doi: [10.1086/166527](https://doi.org/10.1086/166527)
- Ukita, N., & Le Squeren, A. M. 1984, *A&A*, 138, 343
- Ulich, B. L., & Haas, R. W. 1976, *ApJS*, 30, 247, doi: [10.1086/190361](https://doi.org/10.1086/190361)
- VanderPlas, J. T. 2018, *ApJS*, 236, 16, doi: [10.3847/1538-4365/aab766](https://doi.org/10.3847/1538-4365/aab766)
- Wittkowski, M., Boboltz, D. A., Ohnaka, K., Driebe, T., & Scholz, M. 2007, *A&A*, 470, 191, doi: [10.1051/0004-6361:20077168](https://doi.org/10.1051/0004-6361:20077168)
- Xu, S., Zhang, B., Reid, M. J., Zheng, X., & Wang, G. 2019, *ApJ*, 875, 114, doi: [10.3847/1538-4357/ab0e83](https://doi.org/10.3847/1538-4357/ab0e83)
- Yoon, D.-H., Cho, S.-H., Yun, Y., et al. 2018, *Nature Communications*, 9, 2534, doi: [10.1038/s41467-018-04767-8](https://doi.org/10.1038/s41467-018-04767-8)

Zhang, B., Reid, M. J., Menten, K. M., & Zheng, X. W.
2012, ApJ, 744, 23, doi: [10.1088/0004-637X/744/1/23](https://doi.org/10.1088/0004-637X/744/1/23)

APPENDIX

A. TEMPORAL VARIATION OF MASER FEATURES IN THE EAVN IMAGES

The spatial and velocity variation of maser features at different epochs were investigated with the “High-Res. Imaging” in Table 1. We used MF1 as the position reference, which was the brightest and compact maser feature during the period from $\phi = 1.88$ to 3.17, to register the EAVN maps at different epochs. The registration accuracy can be expressed as $\sigma_{registration} = \sqrt{\sigma_{thermal}^2 + \sigma_{structure}^2}$, which includes the thermal noise ($\sigma_{thermal}$) in the interferometric images determined by an elliptical Gaussian fitting with the AIPS task “SAD”, includes error from maser structure ($\sigma_{structure}$) estimated by the blended peak components as shown in Figure 15, and doesn’t include other calibration effects for MF1. When MF1 was not available, we used MF2 instead, and corrected the position offsets using the bona-fide astrometric measurements in Table 4. The registration error is typically ~ 0.1 mas for using MF1 cases ($\sigma_{thermal} \simeq 0.02$ mas, $\sigma_{structure} \simeq 0.05$ mas) and ~ 0.2 mas for using MF2 cases ($\sigma_{thermal} \simeq 0.07$ mas, $\sigma_{structure} \simeq 0.15$ mas). These registration errors are used as the prior errors in the astrometric fitting.

Figure 15 shows the spatial and velocity variation of maser features. Here we found the following four points. Firstly, the shapes of the maser structures generally correlate with the direction of expansion. Figure 16 also shows the complex variation of the interior structure, such as rotation of MF1, expansion on the shape of MF2, sub-structure flashed on MF4, direction changed on MF3 and MF13. Secondly, as shown in Figure 15 and Table 2, the relative proper motions are not necessarily consistent between different Cycles for some maser features. The absolute proper motions and possible accelerations are discussed in section 3.3. Thirdly, as shown in Figure 15 and Table 2, almost all of the maser features have the radial velocity drifts. Generally, the red-shifted maser features are further red-shifted, while the blue-shifted features are further blue-shifted. The systematic radial velocity drifts of individual maser features were found with amplitudes of $< 1.3 \text{ km s}^{-1}\text{yr}^{-1}$, which is consistent with the case of RT Vir (Imai et al. 2003). The radial velocity drifts are not consistent between different Cycles, which shows the gradual behaviors related to the pulsation phases. For instance, the mean of the drifts in Cycle 2 ($\phi 1.89 \sim 2.29$) is larger than that over all the cycles. Finally, the brightest flux density of each maser feature appears at different Cycles in Figure 15, such as MF[3,4,8,12] appear in Cycle 1 ($\phi 1.00 \sim 1.25$), MF13 appears in Cycle 3 ($\phi 2.89 \sim 3.17$) and others appear in Cycle 2 ($\phi 1.89 \sim 2.29$). In Cycle 2 ($\phi 1.89 \sim 2.29$), most of maser features are detected and they all peak on 2020 January 10 ($\phi = 2.00$), except for MF8 and MF16 that are located far from the central star.

As shown in Figure 5, we have further investigated the coherent variation among clusters of maser features located at different projection distances from the central star. In Cycle 2 ($\phi 1.89 \sim 2.29$), there is no noticeable difference in the phase lags of flux variation between different regions. In Cycle 1 ($\phi 1.00 \sim 1.25$) & 3 ($\phi 2.89 \sim 3.17$), the peak flux densities appear at different time for different regions, with no obvious systematic behavior.

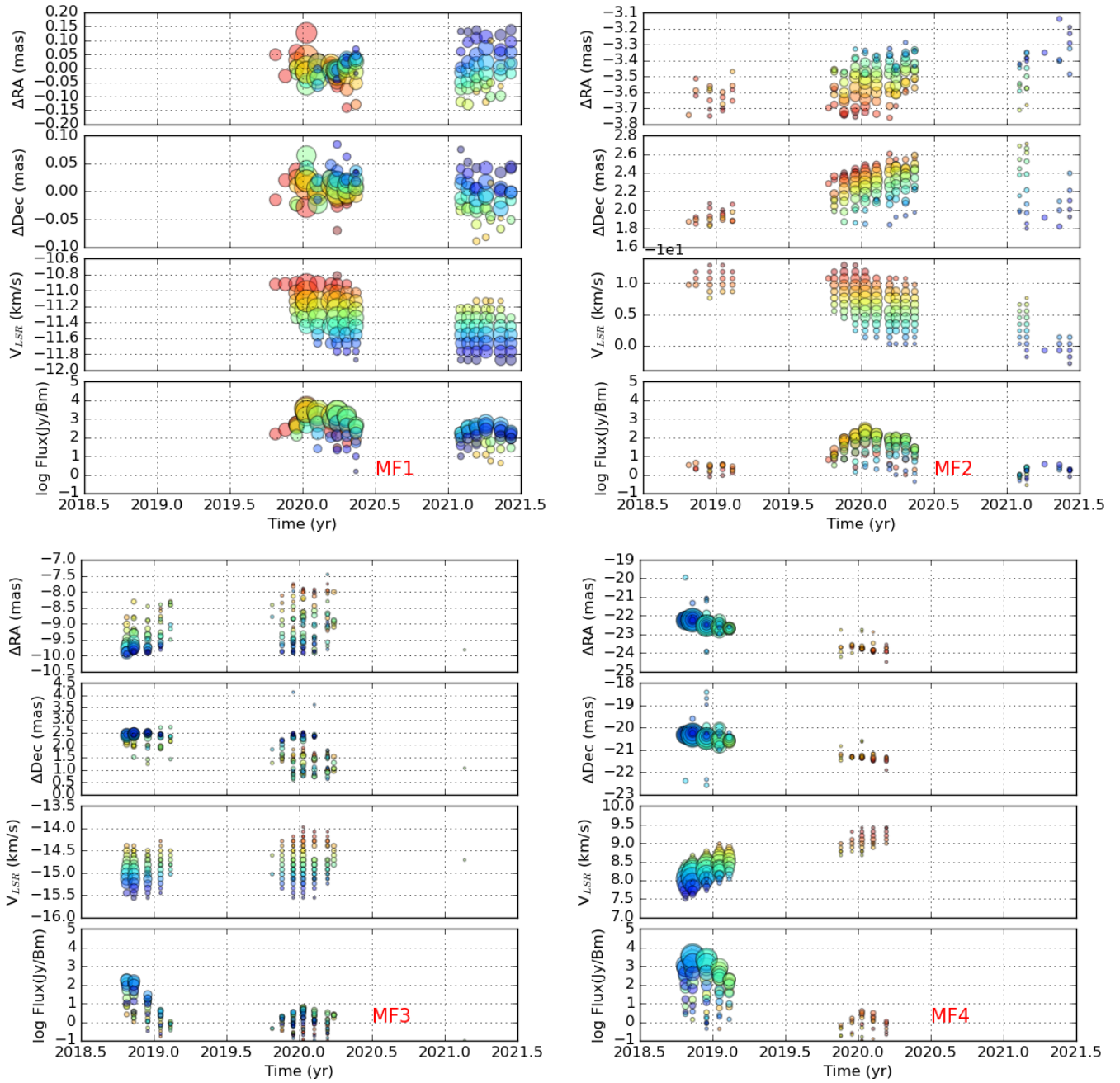


Figure 15. Temporal variation of the internal maser features. The size of the circle indicates the logarithm of the flux density of the maser spot (see the fourth sub-panel for the each maser feature as a legend). The color of the circle indicates the LSR velocity of the spot (see the third sub-panel).

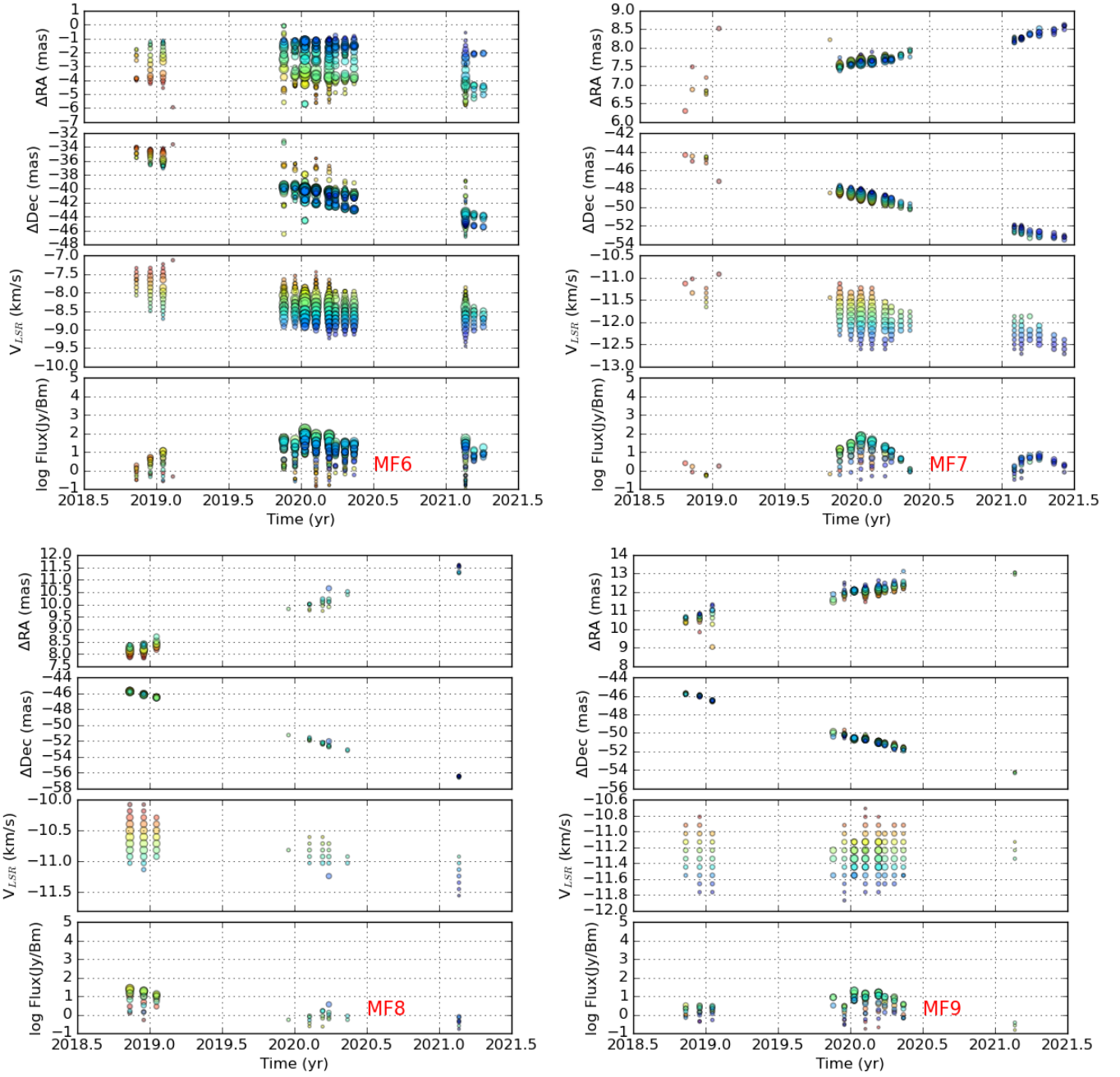


Figure 15. — continued.

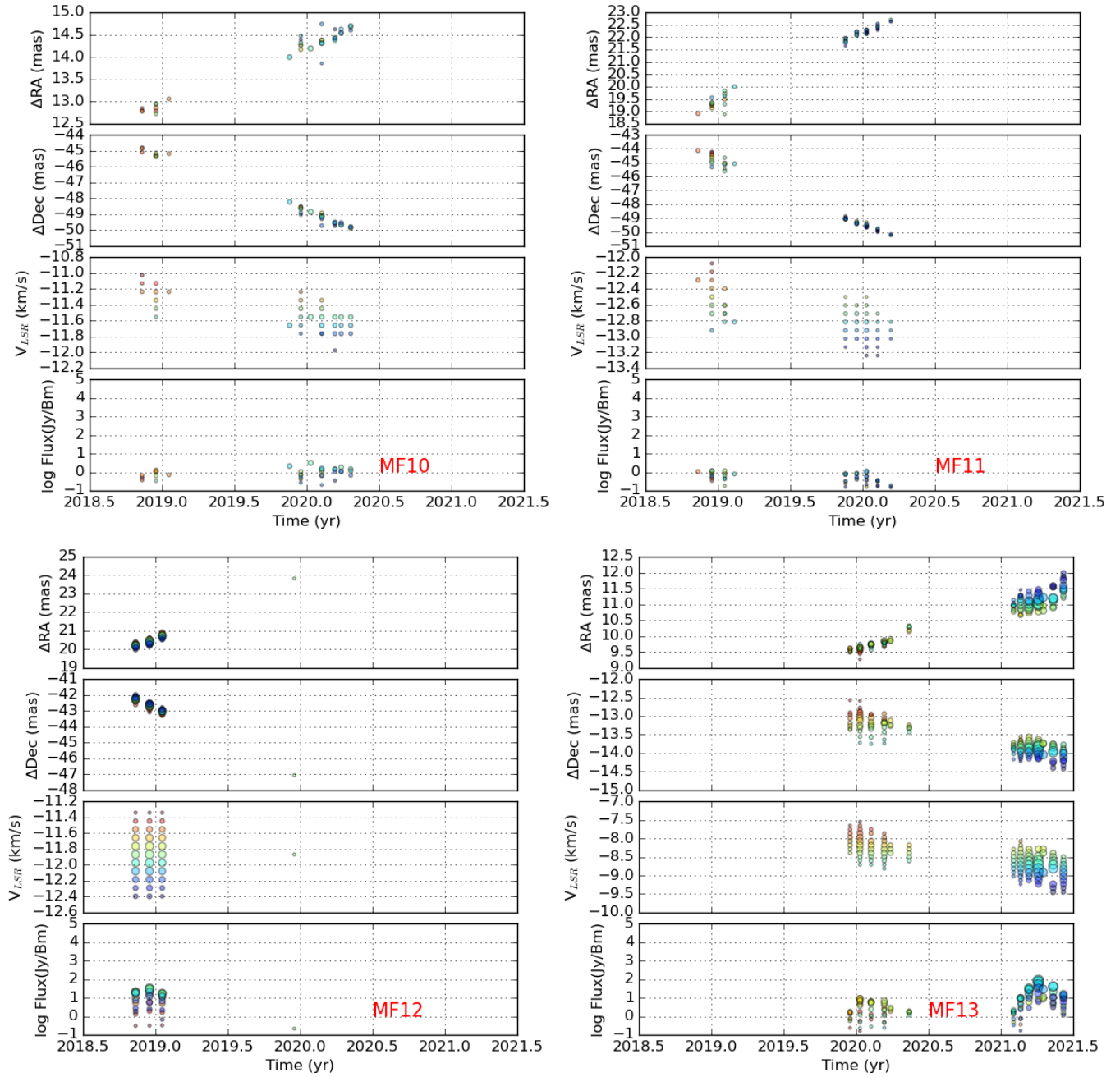


Figure 15. — continued.

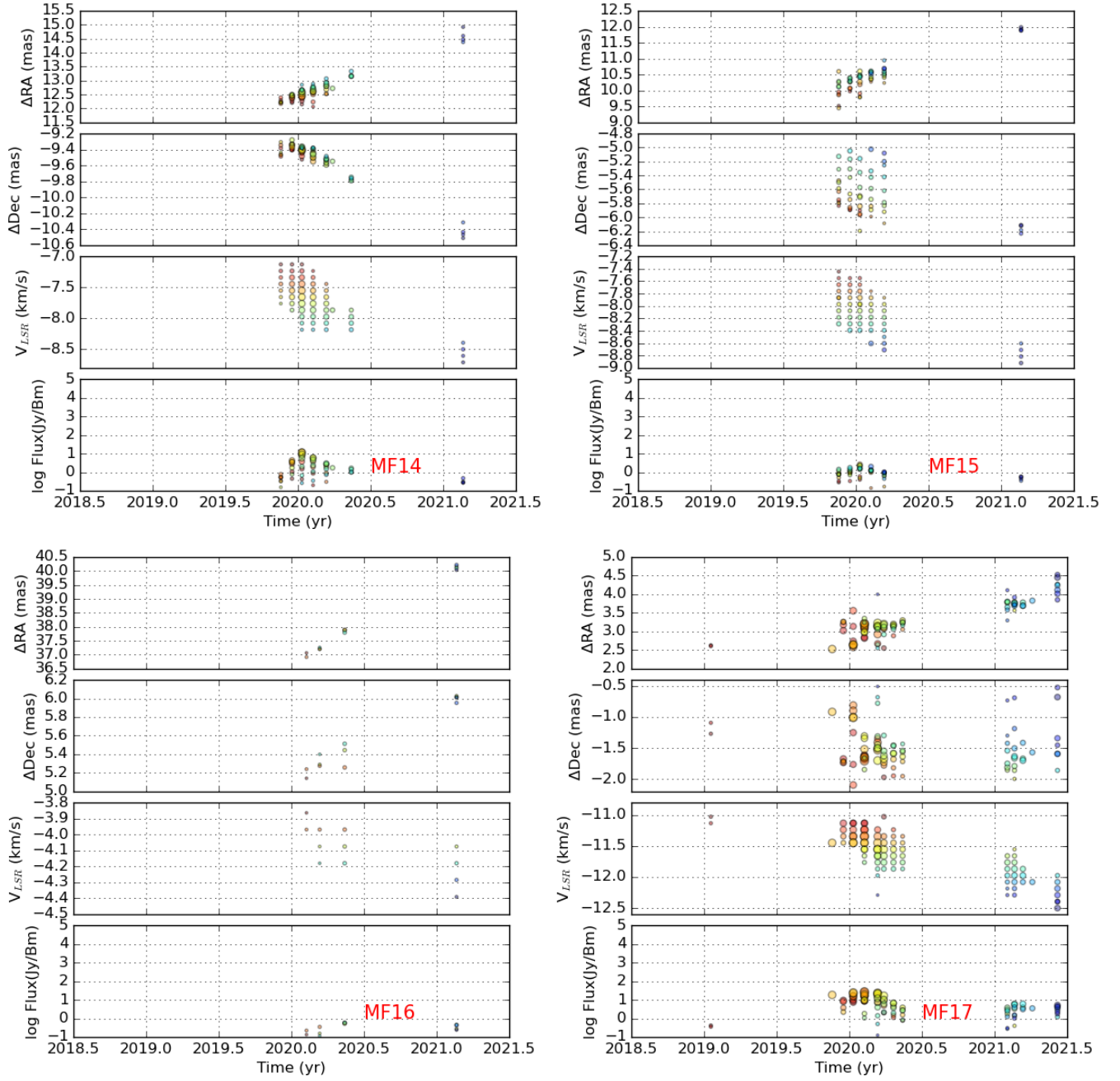


Figure 15. — continued.

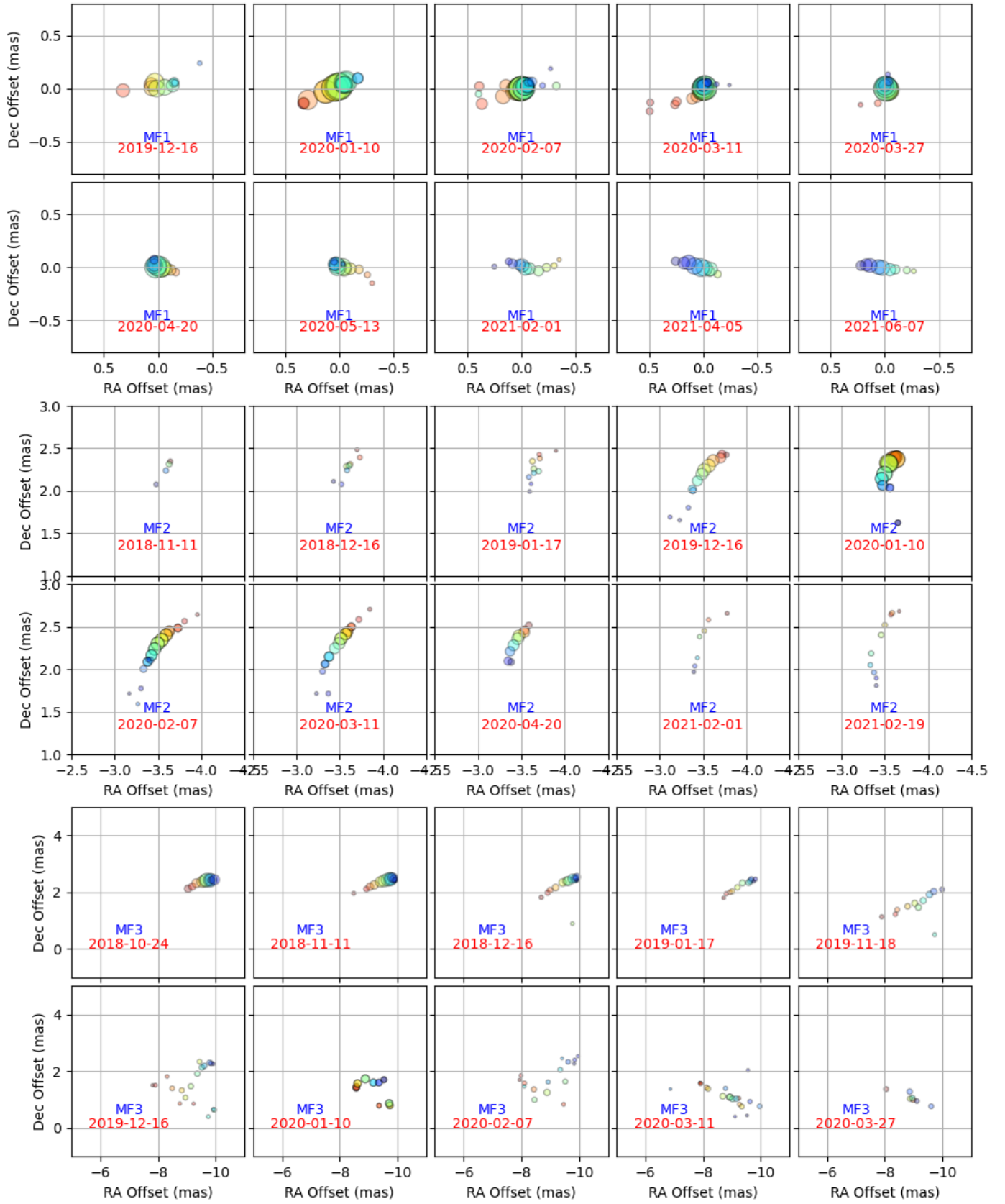


Figure 16. The morphology of individual maser features. The color and size of maser spots are the same to Fig 15.

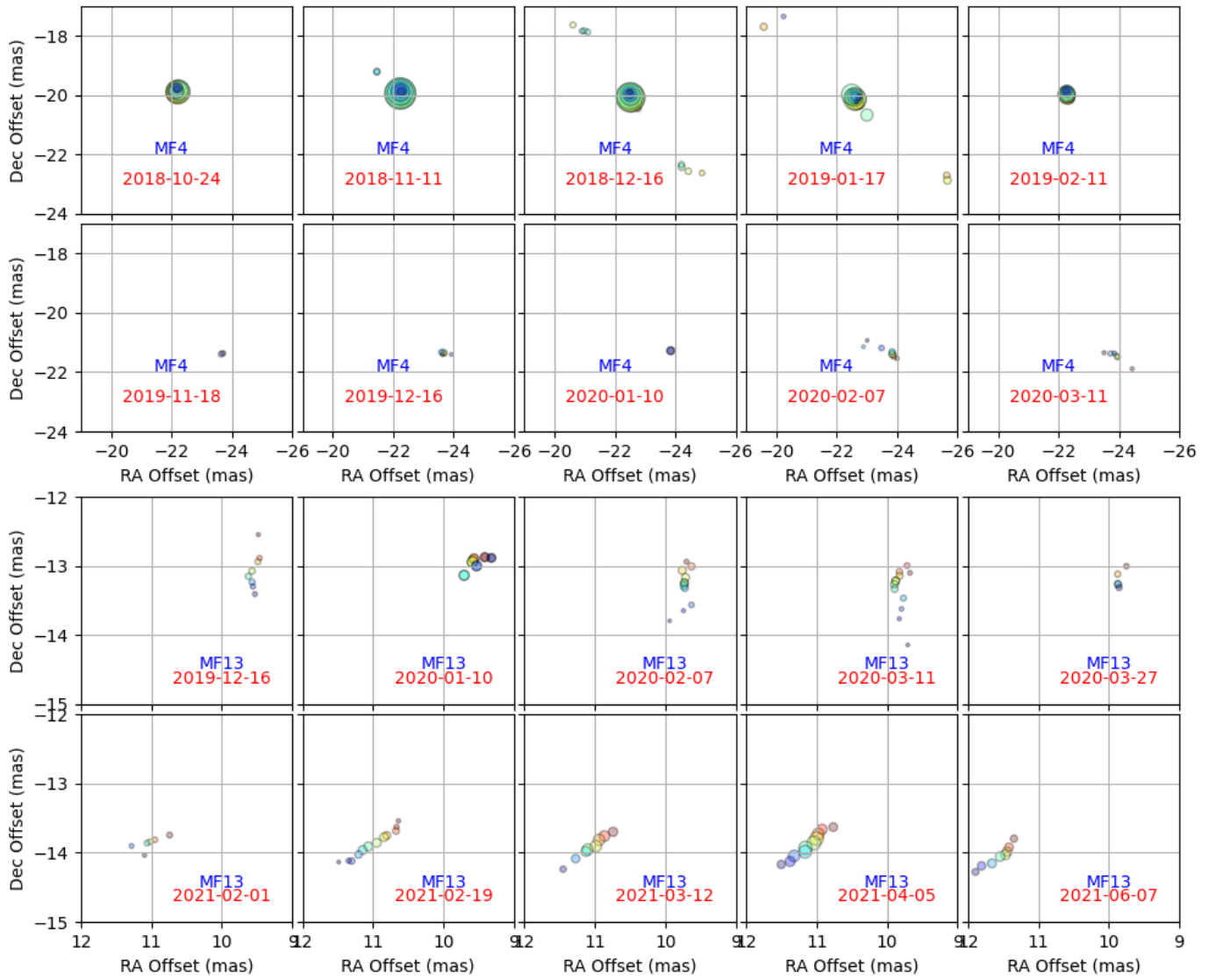


Figure 16. — continued.